EXPERIMENTAL STUDIES OF PULSATILE FLOW PASSING SIDE WALL BIOLOGICAL CAVITIES AND FLOW ENHANCEMENT USING HYDROPHOBIC SURFACES

A Thesis
Submitted to the Graduate Faculty
of the
North Dakota State University
of Agriculture and Applied Science

By

Benjamin Kirk Eichholz

In Partial Fulfillment of the Requirements
for the Degree of
MASTER OF SCIENCE

Major Department:
Mechanical Engineering

November 2020

Fargo, North Dakota

North Dakota State University

Graduate School

Title

Experimental Studies of Pulsatile Flow Passing Side Wall Biological Cavities and Flow Enhancement Using Hydrophobic Surfaces

By

Benjamin Kirk Eichholz

The Supervisory Committee certifies that this ***disquisition*** complies with North Dakota State University's regulations and meets the accepted standards for the degree of

MASTER OF SCIENCE

SUPERVISORY COMMITTEE:

Dr. Yan Zhang
Chair

Dr. Jordi Estevadeordal

Dr. Yechun Wang

Dr. Yao Yu

Approved:

November 25, 2020
Date

Dr. Alan Kallmeyer
Department Chair

ABSTRACT

Understanding the hemodynamics of the cardiovascular system and associated diseases is important for mitigating health risks. We applied flow diagnostic techniques to investigate pulsatile flow characteristics past sidewall cavities, which have implications to two biomedical problems in the cardiovascular system: sidewall aneurysms and the left atrial appendage. Superhydrophobically-coated mesh diverters and synthetic slippery surfaces were studied for their effects on flow diversion and cavity flow enhancements. The study of pulsatile flow over a coated mesh diverter showed that the formation of the primary vortex was prevented which prevents flow stagnation and downwash flow in the cavity. The second study indicates that the healthy heart cycle is essential to reducing flow stasis inside the left atrial appendage. After applying a synthetic slippery surface to the interior of a side wall cavity model, this surface reduced the wall shear stress and allowed vortical flow to reach deeper into the cavity.

ACKNOWLEDGEMENTS

Firstly, I'd like to thank the American Heart Association under the Institutional Research Enhancement Award 19AIREA34470008 by which this thesis research is supported.

I'd also like to thank my advisor and committee chair, Dr. Yan Zhang. His mentorship and expertise have proven invaluable throughout this research. As well, I would like to thank him for guiding me through my graduate education. During my time at North Dakota State University, Dr. Zhang has afforded me opportunities like attending conferences, working on various interesting projects, and learning new research methods and material that would have previously been impossible for me, and for that I will be forever grateful. Without his support, this research would not have been completed, and my time at NDSU would not have been as enjoyable.

As well, I'd like to acknowledge all the people that I have worked with and who have assisted me throughout my time working on this project. Every one of them has provided useful insight, knowledge, and plenty of time towards my project. I'd like to specifically mention a Ph.D candidate that is also a part of Dr. Zhang's research lab, Ruihang Zhang. She has been my go-to for when I have specific questions about the equipment and programs that are used in the lab and has always been ready and able to help me when I've needed it.

I would also like to thank the rest of my committee members, Dr. Jordi Estevadeordal, Dr. Yechun Wang and Dr. Yao Yu, for their time, constructive comments, suggestions, and critiquing.

And finally, I would like to thank my friends and family who have always had my back and always been there for me, you know who you are. I could not have completed this thesis without their support.

TABLE OF CONTENTS

LIST OF TABLES

Table Page

LIST OF FIGURES

Figure Page

LIST OF ABBREVIATIONS

CFD.....Computational Fluid Dynamics

LA .....Left Atrium

LAA .....Left Atrial Appendage

AFib .....Atrial Fibrillation

ECG.....Electrocardiogram

SHB.....Superhydrophobic

SLIPS .....Self-healing, slippery liquid-infused porous surface

PIV .....Particle Image Velocimetry

Wo.....Womersley Number

Re .....Reynolds Number

ω_Z.....Vorticity Magnitude

KE .....Kinetic Energy

CAD .....Computer Aided Design

Tomo-PIV .....Tomographic Particle Image Velocimetry

CCD .....Charge-Coupled Device

CHAPTER 1. INTRODUCTION

1.1. Objective

Hemodynamics, by definition, is the study of the dynamics of blood flow through the body. Since blood flow is vital to the survival of any living animal, including humans, it is an extremely important topic to research. The study of blood flow can be split into categories based on the conditions in which blood is flowing. This thesis looks specifically at the hemodynamics when flowing through a unique geometry, side wall cavities.

Side wall cavities are defined as structures where there is a chamber or pocket attached to a channel, tube, or similar geometry. These side wall cavities can be found naturally in a few locations inside the cardiovascular system, notably in the form of aneurysms and the left atrial appendage. Both structures are found within the cardiovascular system of humans and are important to study because of their unique location away from the main flow of blood. Due to this, aneurysms exhibit an increased likelihood of rupture as well as an increased likelihood of blood clot formation, and the left atrial appendage exhibits an increased likelihood of blood clot formation while under atrial fibrillation conditions.

The objective of this thesis is to investigate the pulsatile flow characteristics in side wall cavity cases of aneurysms and the left atrial appendage based on an *in* vitro pulsatile flow simulator using planar and tomographic Particle Image Velocimetry. In this thesis, particle image velocimetry (PIV) experiments were performed to investigate the pulsatile flow characteristics over a rectangular side wall cavity model as well as an *in vitro* left heart model. As well, implanted meshes with and without superhydrophobic coatings/SLIPS surfaces were investigated within the rectangular side wall cavity model. The rectangular side wall cavity model is a simplified scaled-up model from the actual aneurysm/LAA sizes while the dynamic similarity parameters were

matched. The *in vitro* left heart model was a 1:1 silicone model of the average human left side of the heart and was analyzed using 3D tomographic PIV. The organization of the thesis can be summarized as follows:

Chapter 1. The objective, background and literature review of the thesis research was summarized

Chapter 2. A breakdown of the PIV study of mesh diversion in the side wall cavity model for aneurysm conditions, including the equipment and methods, as well as results, discussion, and conclusions. This chapter focuses on the phase-to-phase variations of flow characteristics over the rectangular side wall cavity and the impact of a regular mesh and a superhydrophobic surface coated mesh on the cavity flow.

Chapter 3. Looked at the PIV study of flow structures in side wall cavity models strictly in atrial fibrillation flow conditions. This includes the equipment and methods alongside the results, discussion, and conclusions. This chapter focuses on the atrial fibrillation flow conditions experienced in the left atrium and left atrial appendage by using both the rectangular side wall cavity model and the *in vitro* silicone left heart model.

Chapter 4. Summarized the PIV study of flow structures with the SLIPS surface insert in the simplified rectangular side wall cavity model in atrial fibrillation flow conditions. This chapter goes over the equipment, methods used, results, discussion, and conclusions of this study and focuses on the phase-to-phase variations of flow characteristics inside the rectangular side wall cavity model and the impact of the SLIPS surface insert lining the walls of the cavity.

The thesis will conclude with a section on future work, areas of improvement, limitations, and a summary of conclusions to be expanded upon and discussed.

The similar geometries between aneurysms and left atrial appendage, meaning that they can be modeled in similar fashion, are the common linkage between the different studies discussed in this thesis. Common issues associated with both are also similar and point towards the ability to similarly model them: both have an increased likelihood of blood clot formation inside of them. Aneurysms have that additional risk of an increased likelihood of rupture. The first study (Chapter 2) looks specifically at aneurysms under normal heart conditions. The other two studies look specifically at the left atrial appendage under normal and atrial fibrillation heart conditions, with the difference between the two being that the third study (Chapter 4) looks at enhancing flow observed in the second study (Chapter 3).

1.2. Background and Literature Review

The cardiovascular, or circulatory system, is the organ system that carries blood throughout the body. Blood is pumped throughout the body by the heart via a system of blood vessels [1]. The heart itself is the central part of the cardiovascular system, and it is broken up into four chambers: the left and right atria and left and right ventricles, and a basic layout of the whole system can be seen in Figure 1 [2].

Blood rheology is the study of blood and its elements, and changes to the properties of blood play a significant role in disease processes. The viscosity of blood is determined by plasma viscosity, the volume fraction of red blood cells, and the mechanical properties of red blood cells. And, because of the mechanical properties of red blood cells, blood behaves as a non-Newtonian fluid, and blood becomes less viscous at high shear rates, or with increased flow through the cardiovascular system [3].

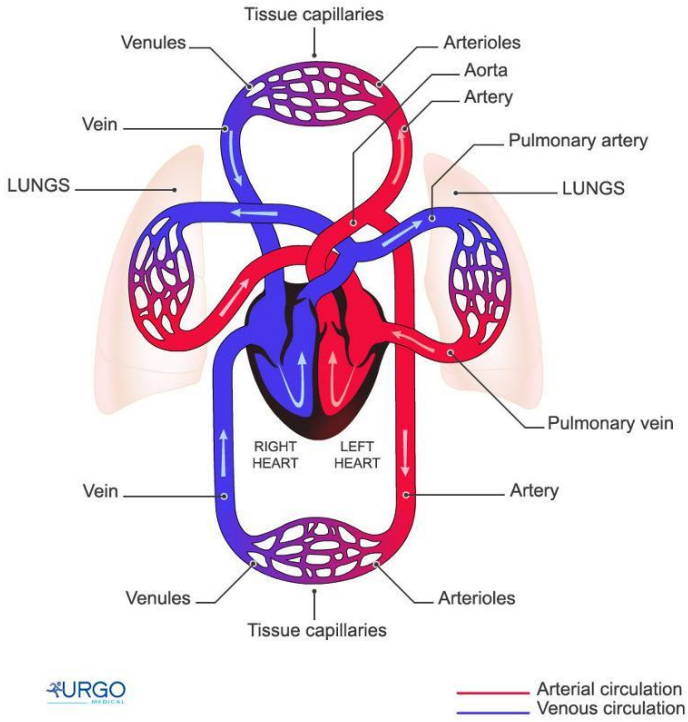

Figure 1. Basic Layout of the Cardiovascular System [4]

Reynolds and Womersley numbers are the only nondimensional parameters required for dynamic similarity in internal pulsatile flow experiments [5]. Womersley number is the relation between pulsatile flow frequency to viscous effects of the fluid flow, and Reynolds number is the relation of inertial forces in a fluid to viscous forces. Normal arterial Womersley numbers range from 4.7-13.0 depending on the size of the artery [6], and left atrium Womersley numbers range between 10 and 20 [5,6]. Average Reynolds number in veins/arteries and the heart tend to be ~100 and ~1000, respectively [7, 8].

There has been a lot of previously completed hemodynamics research, both using computational fluid dynamics (CFD) and experimental studies. As is the case in Hoi, Y., CFD simulations and experimental studies involving hemodynamics are used because of their non-invasive alternative to *in vivo* measurements to estimate hemodynamic parameters. As well, they can be altered from a general form to be more patient-specific than in medical studies [9]. As well,

in vivo measurements of blood velocity profiles are difficult to obtain and interpret, and because of this *in vitro* flow models have often been better to understand vascular hemodynamics [10].

1.2.1. Aneurysms

Aneurysms form on the blood vessels themselves and take on the appearance of an outwardly bulging bubble on the vessel, and they are caused by a localized weak spot on the vessel wall [11]. One risk of aneurysms is that they are prone to rupture, which can lead to uncontrollable bleeding inside the body. The neck of the aneurysm is most at risk because of the combination of thin wall thickness and high wall shear stress due to the blood flowing past and into the aneurysm. Figure 2 depicts a general blood vessel with an aneurysm. Another risk is that blood flow can stagnate inside the aneurysm and form an embolism, or a blood clot. These blood clots can detach from the aneurysm and travel to other parts of the body which could lead to a heart attack or stroke [12]-[14].

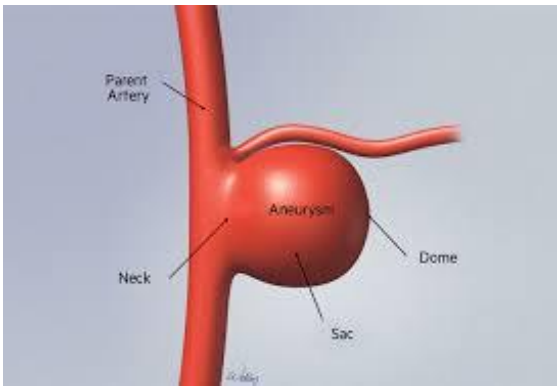

Figure 2. Illustration of a General Blood Vessel with an Aneurysm [15]

Endovascular flow diversion is an increasingly popular treatment option for large cerebral aneurysms because of its effectiveness and minimally invasive nature [16]-[19], compared with traditional surgical clippings and coil embolization [20]. This procedure deploys an expandable mesh structure via a catheter over the neck of the aneurysm to divert the blood flow away from the sac, as illustrated in Figure 3. Early experimental results suggest the placement of a mesh

redirected most of the flow away from the cavity and reduced the hemodynamic loading on the cavity walls [21]-[23]. Consequently, it reduces the risk of rupture and allows gradual intra-aneurysmal embolization and resorption to occur while also preventing leakage of any blood clot inside the aneurysm [24].

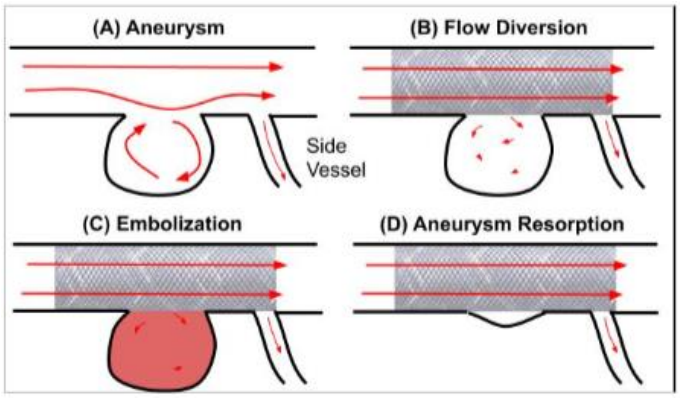

Figure 3. Illustration of Endovascular Flow Diversion

In the case of aneurysms, despite endovascular treatments (Figure 3) being a promising clinical intervention strategy, they currently face some technical barriers. First, stents/grafts are sensitive to platelet activation and protein binding, in part because of the induced shear stress on the device's surfaces, which lead to thrombus and plaque formation and increased arterial stenosis [16], [25]. Patients who received endovascular treatments require life-long anticoagulant medication to mitigate their risk of arterial stenosis and stroke [26]. Second, the deployment of diverters sometimes causes significantly altered local hemodynamics, which may result in life-threatening rupture events during or after procedures [27].

There have been several studies to begin with that utilize PIV to study models of side wall aneurysms [8, 26-31]. Most of these previous studies compare PIV results with CFD results and generally find a good relationship between those results [28, 31]. Each of these studies show the same general flow inside the aneurysm with a clockwise rotating swirl being induced within.

However, studies involving the hemodynamics of mesh flow diverters across aneurysms are even less common. These mostly consist of purely CFD studies [19, 32, 33]., in a recent CFD study, Dholakia et al. [19] claimed that "there is poor standardization of study variables" in terms of interpreting the hemodynamic effects of the mesh flow diverters. There are also some *in* vitro PIV studies that look at flow diversion in aneurysms [34, 35]. However, they utilize non-physiological flow conditions [35] and don't mention the technical barriers faced by endovascular flow diversion techniques [34, 35].

1.2.2. Superhydrophobic Coatings

The proposed superhydrophobic (SHB) mesh is motivated by the superior biological (anti-platelet [36]) and fluid dynamic (drag-reducing [37]) properties of SHB surfaces and their potential to provide transformative solutions, overcoming the current technical barriers of flow diversion treatments. Superhydrophobic surfaces repel water and water-based liquids because of the micro-surface structures. This is done through the creation of an air-liquid interface being created by the micro-surface structures. The-low-surface energy creates slip wall boundaries, which dramatically reduce surface friction and flow drag [37]. An illustration of the structure of these hydrophobic coatings can be seen in Figure 4. Hydrophobic coatings in general increase the contact angle of a water droplet on a surface. Superhydrophobic coatings are unique in the way that this contact angle exceeds 150° [38].

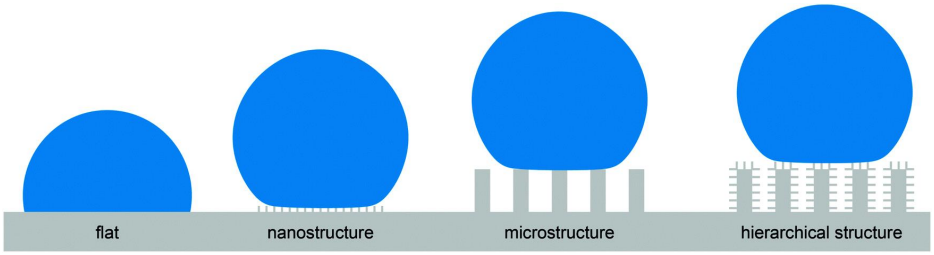

Figure 4. An Illustration of the Structure of Hydrophobic Coatings [39]

And, in recent years, SHB materials have been studied in a variety of in vitro biomedical applications. The anti-adhesion property of SHB surfaces made them attractive in applications in which protein and bacteria adsorption to biomaterial surfaces need to be inhibited [40]-[42]. SHB surfaces are also incorporated in microfluidic devices to control flow in lab-on-a-chip diagnostics [43] and in drug delivery platforms to enable more efficient delivery of therapeutic agents [44]. Novel flexible tubes made from SHB-materials show significant drag reduction and excellent self-cleaning properties: in a sliding and free falling water droplet experiments, SHB tubes showed an up to 5000 times increase in droplet acceleration and 99% friction reduction [37]. SHB polydimethylsiloxane (PDMS) tubes with titanium-oxide layers also showed excellent blood repellency and sliding blood droplets on an inclined tube did not leave any blood stain [37]. Recently, the potential application of SHB coating on mechanical bi-leaflet prosthetic heart valves have been investigated [45] via a bioengineering experiment. The work showed dramatically reduced cell adhesion and minimized fluid shear stress on the mechanical heart valve, indicating its potential for reducing the thrombotic risk caused by blood-material interactions.

Using hydrophobic or similarly superhydrophobic surfaces coatings for various uses in the medical field has been around for about a decade. This includes coating the tops of various medical devices with hydrophobic coatings [46]. As well, stents having hydrophobic properties have been studied [47, 48], but how these properties modify the flow of blood through a vessel has not been investigated. And to the best of our knowledge, no studies have investigated the effects of hydrophobic coatings on mesh flow diversion for aneurysms.

1.2.3. Left Atrial Appendage

The left atrium is one of the four chambers of the heart, and it receives newly oxygenated blood from the lungs via the four pulmonary veins, denoted as the left and right superior and

inferior pulmonary veins (LSPV, LIPV, RSPV and RIPV) with two veins bringing newly oxygenated blood from each lung. It is connected to the left ventricle by the mitral valve.

The left atrial appendage (LAA) is a small, ear-shaped pouch that can be found high on the body of the left atrium. Its physiological function is to serve as a decompression chamber during the systolic portion of the heartbeat, when left atrial pressure is high [49]. It also often serves as an approach for surgery involving the mitral valve, which is connects the left atrium and left ventricle [50]. A model of the left side of the heart, including the left atrium and LAA can be seen in Figure 5.

During a normal heartbeat, the LAA functions without an issue. However, during atrial fibrillation, blood flow may stop flowing into and out of the LAA, which can lead to the formation of a blood clot [49].

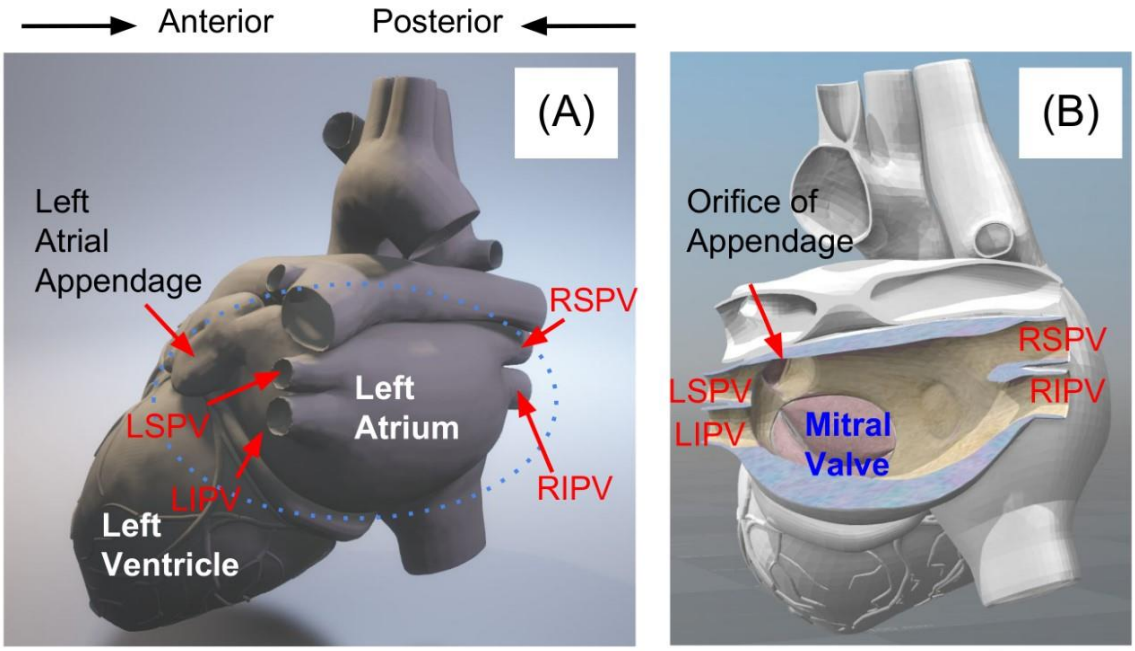

Figure 5. A Model of the Left Side of the Heart

Atrial Fibrillation (AFib) is an abnormal heart rhythm characterized by the rapid and irregular beating of the atria [51]. AFib is estimated to affect between 2.7 million and 6.1 million

people in just the United States, and it is the most common type of arrhythmia worldwide [52], [53]. AFib is caused by the regular impulses produced by the sinus node, which acts as the heart's natural pacemaker, being overwhelmed by rapid discharges from the atria. This results in irregular and random electrical signal pathing to the atrioventricular node, which electrically connects the atria to the ventricles [54, 55]. The result of this is the rapid atrial rhythms that disrupt the normal beating of the heart. Figure 6 depicts normal electrical pathing compared with the abnormal electrical pathing of AFib, along with accompanying electrocardiogram (ECG) records, which monitor the electrical signal from the heart.

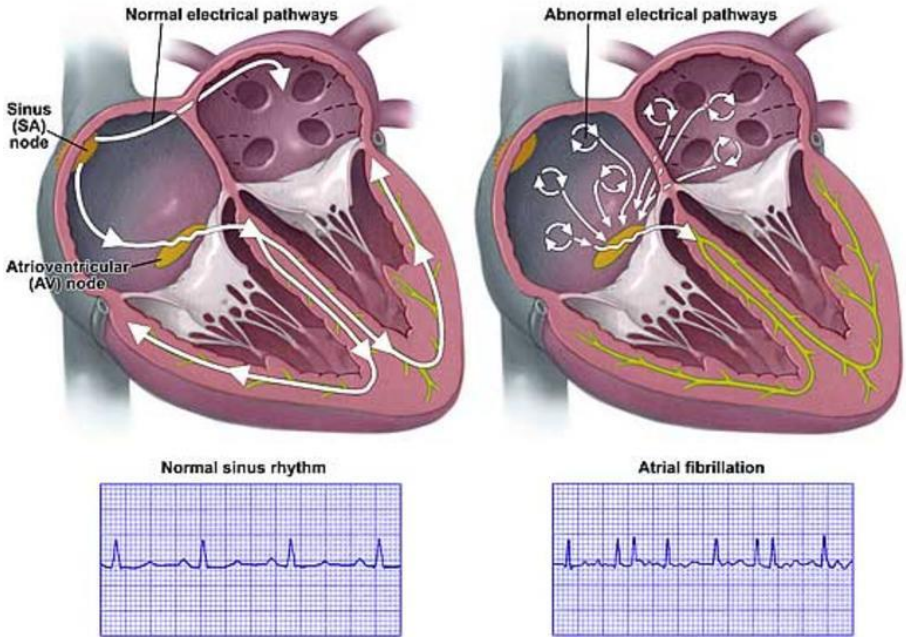

Figure 6. A Comparison of Normal and AFib Electrical Pathways and ECG Records [56]

The variables known to cause blood clot formation, like LAA size and flow pattern are all known to be changed due to AFib [49]. And it is estimated that about 90% of the blood clots that cause strokes develop within the LAA [57]. However, implants can be used as left atrial appendage closure devices (WATCHMAN^{TM}, Boston Scientific), which is designed to prevent leakage of blood clots and subsequent stroke in patients with atrial fibrillation [58].

Implants like this are used to completely close the LAA in patients with AFib to prevent blood clots from forming [58]. However, after the implant has been placed in the LAA, blood clots may form on the surface of the implant, which may later detach and cause a stroke [57]. As well, by completely blocking off the LAA, the functionality of it being a decompression chamber during periods of high pressure in the heart is lost [49].

Like the aneurysm case, *in vitro* studies looking at flow inside the left atrial appendage are mostly limited to CFD [59, 60]. And all indicate the left atrial appendage to be associated with a higher risk of blood clot formation. Particle image velocimetry cases involving the left atrial appendage are seldom found, with only one other group looking at flows in an anatomically shaped left-atrium [61]. However, they stated that further studies including multi-planed three components PIV are necessary to correctly visualize the flow through the left atrium. To the best of our knowledge, there is not any other literature looking at enhancing the flow inside of the left atrial appendage using a hydrophobic or similar surface.

1.2.4. SLIPS Surface

Hydrophobic surfaces, in general, can still show some problems that can restrict their applications, most notably, their failure to maintain the air-liquid interface between the surface and in this case, the water droplet, as well as a reduction in usefulness upon physical damage. The trapped air in the structured solid shown in Figure 4 is there to act as a cushion to the liquid on top, and liquids can easily penetrate this layer, breaking it down [62]. Because of this, a self-healing, slippery liquid-infused porous surface (SLIPS surface) was also analyzed for use in these experiments. SLIPS surfaces have been shown to have excellent omniphobic properties and exhibit low contact angle hysteresis and low sliding angles [63, 64] The SLIPS surface uses a nano/microstructured substrate to lock in place a fluid to form a liquid-liquid interface between

the surface and in this case, the water droplet [63]. As well, it has been shown that SLIPS surfaces can keep their properties, even after withstanding both laminar and turbulent flows for a significant period of time [65]. However, no studies use a SLIPS surface to enhance stagnated flow inside of a cavity.

The SLIPS surface utilizes a low-surface-energy structured material, a porous Teflon membrane, and infuses it with an inert lubricating fluid. This inert lubricating liquid has preferential wetting to the Teflon compared with water and does not easily break down under flow. This combination forms a stable slippery surface that acts similarly to (super)hydrophobic surfaces. This surface exhibits a more stable barrier between the surface and the liquid, and therefore is less likely to breakdown under pressure or physical damage [63]. An illustration of the SLIPS surface can be seen in Figure 7.

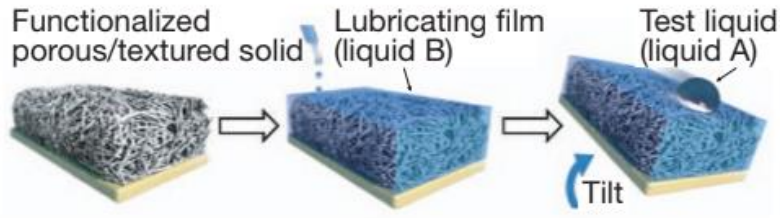

Figure 7. An Illustration of the SLIPS Surface [63]

CHAPTER 2. PIV STUDY OF MESH DIVERSION IN THE SIDE WALL CAVITY MODEL FOR ANEURYSM CONDITIONS[1]

2.1. Chapter Overview

Pulsatile flow over an open cavity represents one type of physiological phenomenon related to cerebral sidewall aneurysms. In recent years, endovascular treatments using mesh-based implants have become increasingly popular. In this study, we investigate the characteristics of pulsatile flow over a simplified sidewall cavity under specific Reynolds/Womersley number conditions using Particle Image Velocimetry. The impacts of a regular mesh and a superhydrobobically-coated mesh on the cavity flow are investigated. Our results quantify the phase-to-phase changes of the flow fields and reveal the formation and the transport of the primary vortex over the ostium of the rectangular cavity. Results suggest the meshes diverted the main flow away from the cavity and prohibited the development of the primary vortex. A penetrated jet flow was formed near the front side of the cavity due to the presence of the mesh. The superhydrophobic mesh dramatically reduced the kinetic energy of the penetrated jet into the cavity. It indicates the mesh flow diversion is effective because of the destruction of the shear-induced vortex dynamics that causes flow stagnation on the rear cavity wall. Our results also indicate the superhydrophobic coating is potentially beneficial in terms of reducing the hemodynamic loading inside the cavity.

[1] The content in this chapter was co-authored by Benjamin Eichholz, Ruihang Zhang and Dr. Yan Zhang and was also published and copyrighted by ASME under the title "Diversion of Pulsatile Flow Over a Rectangular Sidewall Cavity Using Superhydrophobic Mesh." For this chapter specifically, Benjamin Eichholz had the primary responsibility for constructing the models, running experiments, gathering data, developing conclusions, and drafting of the chapter itself. Ruihang Zhang assisted with experimental setup and data acquisition, and Dr. Yan Zhang assisted with data processing and proofreading of the chapter.

2.2. Materials and Methods

2.2.1. The Pulsatile Flow Simulator and Cavity Model

A closed-loop cardiovascular flow simulator, as illustrated in Figure 8, was used to provide flow conditions for this experiment. The pulsatile flow was generated by a programmable piston pump (PD-1100, BDC Laboratories). A pump head module equipped with a left ventricular diastole module (BDC Laboratories) was connected to the pump to generate the tuned flow outputs. Compliance and resistance units were used downstream of the test model to tune pressure-flow conditions. A fluid tank was used upstream of the pump head to receive the return flow and a magnetic stirrer was used to mix the PIV seeding particles.

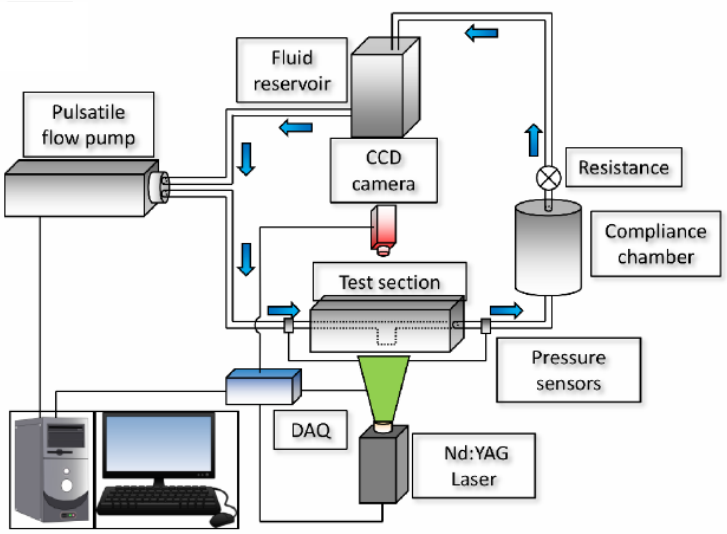

Figure 8. Schematic of the Closed-Loop Cardiovascular Flow Simulator

The working fluid is a mixture of water and glycerin with a volumetric ratio of 0.67:0.33. The mixture has a density and dynamic viscosity that closely resembled the properties of blood plasma. The non-Newtonian property of blood was not considered in this study. The flow rate and frequency of the flow was set to provide appropriate Reynolds and Womersley numbers for the dynamic similarity of a large cerebral aneurysm flow [66]. The two dimensionless numbers are defined as, and, respectively, where is the width of the channel (0.025 m); u represents the average

velocity of the flow; represents the density of the working liquid; is the dynamic viscosity and is the angular frequency of the pulsatile flow. More details regarding the simulator can also be found in [67]. A square channel with a rectangular sidewall cavity model with aspect ratio of 1.5 (depth/width) was constructed using acrylic sheets, as shown in Figure 9.

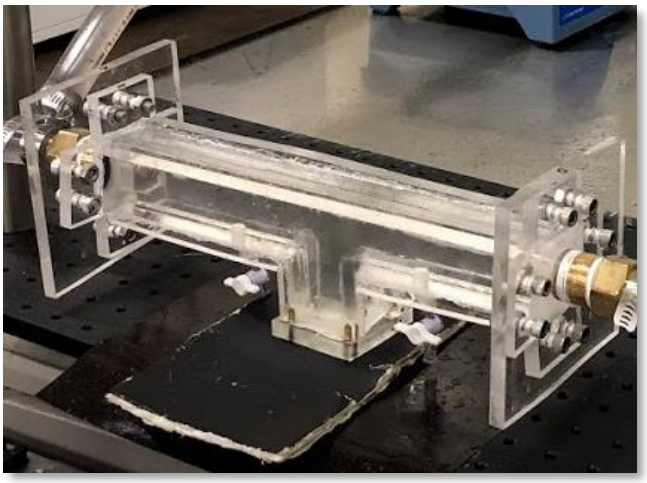

Figure 9. Rectangular Sidewall Cavity Model

The width (D) of the channel and the cavity (L) are both 1 inch (25.4 mm) and the depth (H) of the cavity was 1.5 inches (38.1 mm). The geometric scale of the model is approximately 10:1 if considering an aneurysm ostium size of 2-3mm and approximately 2:1 if considering a left atrial appendage ostium size of 12-16 mm. The aspect ratio was selected according to the clinical finding of the statistical threshold [68], [69] regarding aneurysms rupture, which suggests that an aspect ratio greater than 1.6 is associated with increased risk of aneurysm rupture. Dimensions are detailed in Figure 10.

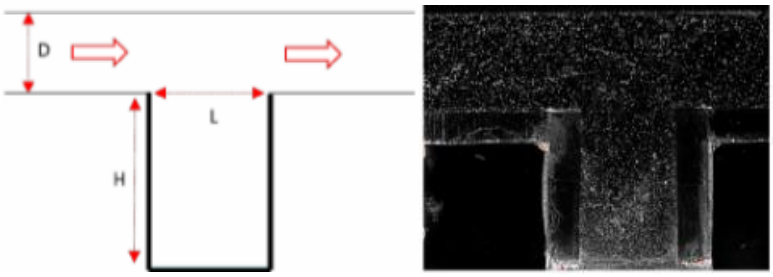

Figure 10. Schematic and Picture of the Cavity Model

2.2.2. Waveform Models

The waveform utilized for aneurysm flow comes from the built in, programmable waveform of the pulsatile flow pump through a user-defined skewed sinusoidal function. In the experiments, a time ratio of 40% between systolic (contraction) and diastolic (relaxation) period was programmed to the pump to generate a physiological flow waveform [70].

It is also important to note the Womersley Number. The Womersley Number (Wo), as mentioned previously, is a dimensionless number used in biofluids that shows the relationship between pulsatile flow frequency and viscous effects of the flow. It is very important to match the Womersley number between the experiments done in this study to the Womersley number found in real-life cases to achieve dynamic similarity in the flow. The Womersley number and other similarity parameters is presented in Table 2 in the Results section.

2.2.3. Mesh Structure and Superhydrophobic Coating

An aluminum wire mesh with diamond-shaped pores was used to model the flow condition induced by flow diverters (Figure 11a). The mesh has a porosity (total pore areas/total area) of 70% and a pore density of 9.4 pores/cm^2. The weave pattern and porosity of the mesh closely resemble those in commercial flow diverters [19]. The detailed dimensions of the mesh pores are shown in Table 1. Note that these dimensions were measured from digital images using ImageJ and each dimension was measured from ten sample pores to calculate the average and relative errors. To apply the mesh over the cavity, a square piece of the mesh was cut and inserted into the cavity to cover the cavity ostium.

Table 1. Detailed Dimensions of the Mesh

Pore Density (#/cm^2)	Porosity (%)	Pore Area (mm)	Length L_1 (mm)	Length L_2 (mm)	Length α (deg.)	Angle β (deg.)
9.4	70.0	7.4 ± 0.2	3.4 ± 0.1	3.1 ± 0.1	70.3 ± 2.6	115.9 ± 2.2

The superhydrophobic mesh was prepared by applying a commercial superhydrophobic spray coating (Rust-Oleum® NeverWet®). The spray consists of a base coat of hydrocarbon resin and a topcoat of acetone. The effectiveness of coating was first tested on a flat solid surface. The static contact angle was measured using an optical goniometer, as shown in Figure 11b-d. After the coating was applied, the static contact angle is >150° Figure 11c shows the results of contact angle measurements of the coated surface using different volumetric ratios of water- glycerin mixture. It suggests that the coating exhibited superhydrophocity to varied mixtures and was relative insensitive to the mixing ratio. Figure 11d shows the contact angle of the coated surface remained relatively stable after being pulled out from prolonged water immersion.

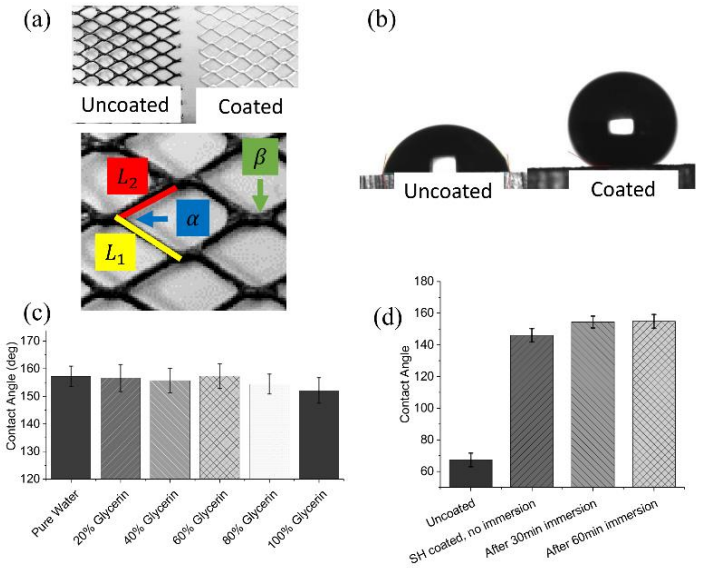

Figure 11. The Mesh Model and Superhydrophobic Coating

2.2.4. Particle Image Velocimetry

A PIV system with a double-pulsed Nd:YAG laser (NewWave Gemini 200, 100mJ, 532nm) was used in these experiments. A set of concave and cylindrical lenses were applied to

convert the laser beams into thin sheets with a thickness of approximately 1mm. The laser sheets pass thought the mid-plane of the simplified rectangular cavity model vertically from the side wall. A 2M-pixel CCD (charge-coupled device) camera was placed on the top of the test section, and the lasers and camera were synchronized by a delay generator (BNC Model 577, Berkeley Nucleonic Corp.), which was externally triggered by the pump digital output signal. The delay to the trigger signals was then controlled specifically for each test case to obtain phase shifts. The uncertainty of the synchronizing (based on the rise time of TTL signal) was less than 3 nanoseconds. The working fluid was seeded with hollow glass microspheres with a seeding density of 0.1 ppm. These particles have an average diameter of 50μm. The Stokes number of the particle flow was much less than 1, which indicates that the particle could follow the flow streamline very well. An illustration of a general PIV setup that can be used to measure flow velocity over time by tracking the glass microspheres through the flow can be seen in Figure 12.

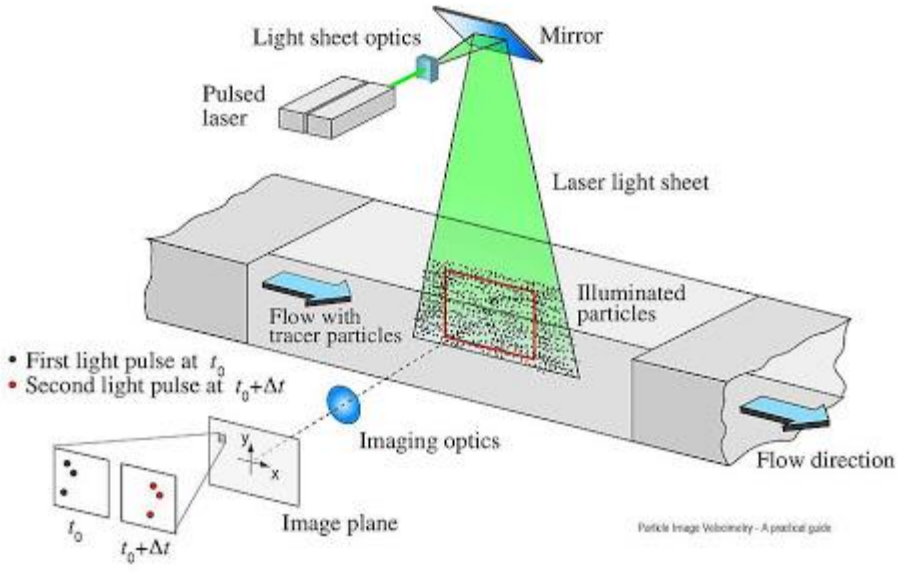

Figure 12. A General PIV Setup [71]

For the post-processing, instantaneous PIV velocity vectors were computed using cross-correlation algorithms provided by the LaVision Davis software. The computation of cross-correlation involved successive pairs of raw images in a multiple-pass process with interrogation window sizes of from 32×32 to 16×16 pixels. An overlap of 50% was used for the cross-correlation and the Nyquist criterion was satisfied. Per cycle, 20 phases for the aneurysm flow conditions were captured, with a sampling rate of 10 frames/sec. One hundred instantaneous velocity samples were captured and used for averaging flow field information for each case.

2.3. Results and Discussion

2.3.1. Pulsatile Flow over an Open Cavity

The flow conditions were simulated in the present study to establish the dynamic similarity for the cerebral aneurysm. Calculated from the PIV results, the bulk average velocity of a cycle (U_{avg}) for the condition is 0.027 m/s. The peak systolic mean velocity is 0.09 m/s. The characteristic length was the width of the channel, i.e. 0.025m. The corresponding dimensionless number for the aneurysm study case is listed in Table 2. Note that the average Reynolds number was calculated based on the bulk average flow velocity, while the peak flow Reynolds number was calculated based on the mean flow.

Table 2. Dimensionless Numbers of the Aneurysm Flow Condition

Case	Average Re	Peak flow Re	Wo
Aneurysm	206	725	6.2

Figure 13 presents the normalized velocity magnitude and normalized out-of-plane vorticity of the sidewall aneurysm case averaged at multiple phases during 10%-60% of the cycle. The vorticity magnitude was calculated using the equation $\omega_Z = \frac{\partial v}{\partial x} - \frac{\partial u}{\partial y}$. The velocity magnitude was normalized by the bulk average velocity of a cycle (U/U_{avg}), while the vorticity magnitude

was normalized using the width of the channel and the bulk average velocity ($\omega_Z L/U_{avg}$). The results show that at the beginning of the systolic phase (10%), a primary vortex with a clockwise rotation was developed due to the shear force between the accelerating main flow and the flow inside the cavity. The vortex then was transported towards the rear side of the cavity and impinged on the rear wall (20%-30%), causing a downwash flow on the back side. At the end of the systole (40%), the primary vortex was enlarged, strengthened, moved out of the cavity due to the deceleration and decreasing pressure in the main flow. The strengthened vortex was evidenced by the increased velocity magnitude near both front and rear side of the cavity ostium. The enlarged vortex persisted but started to dissipate during the early diastolic phases (50%-60%).

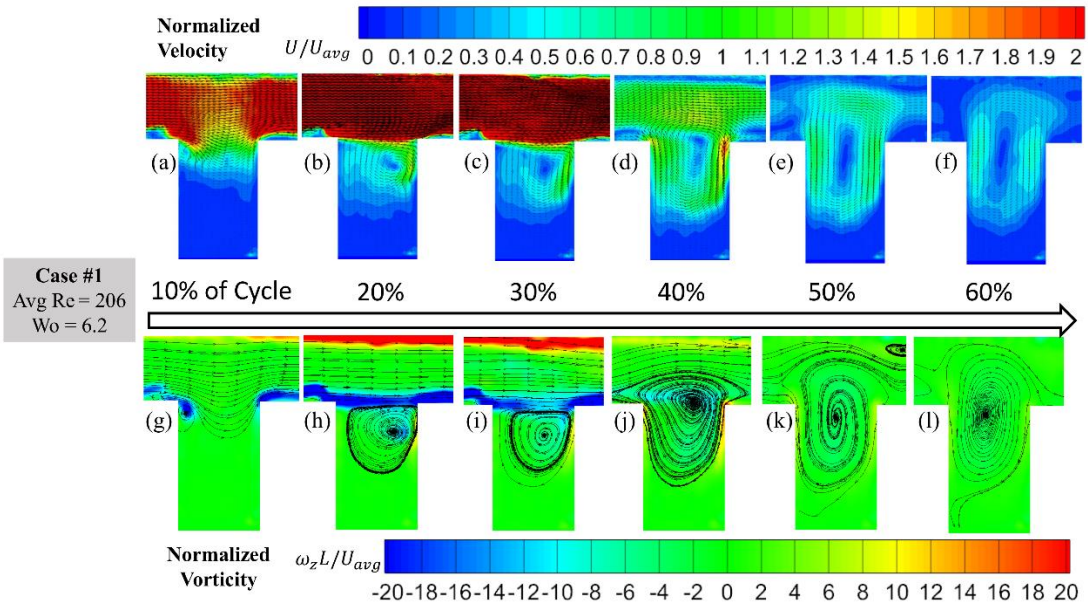

Figure 13. Normalized Velocity & Vorticity Contours of the Aneurysm Flow

2.3.2. Effects of the Mesh Flow Diverter

The effects of the regular mesh and the SHB mesh on the cavity flow are examined. Figure 14 shows the normalized vorticity contours and streamlines near the ostium of the cavity during the systole phases of the aneurysm case. The white dashed line shows the location of the mesh over the ostium. The slight curvature was caused by the force applied to the mesh to firmly attached

it into the cavity. The results show that both mesh diverters significantly altered the hemodynamics around the cavity. The mesh over the ostium diverted the main stream away as evidenced by the altered streamlines and vorticity layers and prohibited the formation of the primary vortex in the meantime. The destruction of shear-induced vortex is particularly beneficial for the aneurysm hemodynamics as it would reduce the pressure and shear stresses on the real wall of the cavity. The presence of the mesh also caused a penetrated jet flow near the front side of the cavity due to the interaction between the main flow and the mesh struct. The penetrated jet also caused a vortex that rotates in counterclockwise direction between the mesh and the jet. Furthermore, the SHB-coated mesh reduced such jet flow penetration as shown by the decreased vorticity magnitudes.

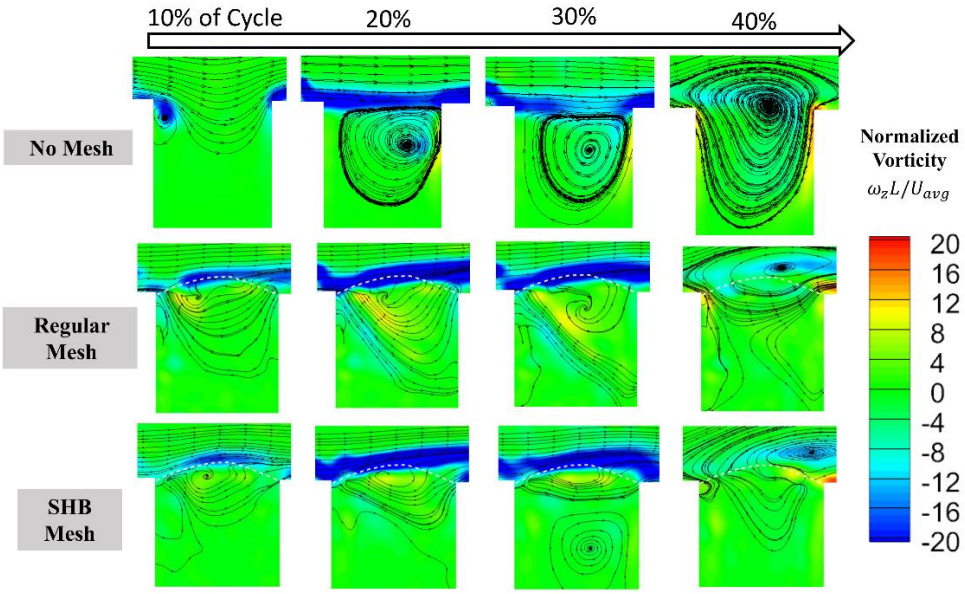

Figure 14. The Normalized Vorticity Fields of Two Mesh Models

The reduction of jet flow penetration can be seen more clearly in terms of specific kinetic energy profiles shown in Figure 15. These profiles were extracted in X direction (horizontally) at 0.2H (depth) below the ostium of the cavity from the PIV results. The specific kinetic energy was defined as the kinetic energy (KE) per unit mass of the flow, i.e., where U is the local velocity magnitude. The results show that in contrast to the no-mesh case where the KE was concentrated

near the rear wall, the regular mesh caused a strong downward jet flow that contributed to an increased KE near the center of the cavity and away from the rear cavity wall. The location of the high KE varied under the flow conditions. Furthermore, the results consistently show that the KE in the cavity with SHB mesh is of order-of-magnitude weaker than the regular mesh and no mesh case.

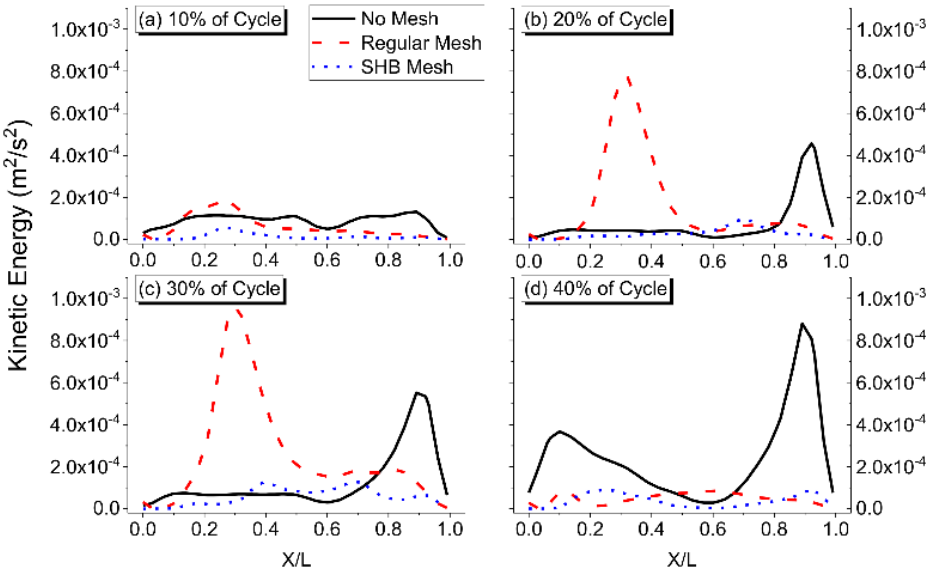

Figure 15. Specific Kinetic Energy Distribution 0.2H Below Cavity Ostium

Overall, the results of this suggest that the presence of the mesh prohibits the formation of the primary vortex and therefore prevents the flow stagnation and downwash flow at the real cavity wall. Instead, the mesh structure promotes the formation of penetration jets near the front side of the cavity, causing the increase of flow kinetic energy near the middle of the cavity ostium. The SHB mesh significantly reduces the penetrated jet flow energy compared to the regular mesh, which might be beneficial to further mitigate the risks of hemodynamic loading immediately after the deployment of the diverter.

2.4. Conclusions

An experimental study of pulsatile flow over a rectangular cavity with different mesh diverters using a cardiovascular flow simulator and particle image velocimetry was performed. The flow condition studied here is: average Re=206, Wo=6.2, to reach dynamic similarity to aneurysm flow. A scaled-up rectangular cavity was used, and aluminum meshes with a porosity of 70% with and without superhydrophobic coatings were deployed over the ostium of the cavity during the experiments. PIV results revealed the formation and transport of the primary vortex over the open cavity and different flow patterns at different phases of the pulsatile flow. The aneurysm flow case showed a persisting primary vortex that was intensified and elevated from the cavity towards the end of the systole and into the early diastole phases. The presence of the mesh diverted the main flow and prohibited the formation of the primary vortices. With mesh implanted, a penetrated jet flow was developed near the front end of the cavity. The superhydrophobic mesh significantly decreased the kinetic energy of the jet flow penetrating the cavity. The results imply potential benefits of superhydrophobic mesh for reducing hemodynamic loading inside the aneurysm cavities after the deployment, besides other anticoagulation, and anti-platelet properties of superhydrophobic surfaces that has been studied by previous research. Future studies are needed to quantify the effects of pore density, porosity, and realistic geometries on the flow diversion outcomes of superhydrophobic diverters.

CHAPTER 3. PIV STUDY OF FLOW STRUCTURES IN SIDE WALL CAVITY MODELS IN ATRIAL FIBRILLATION FLOW CONDITIONS

3.1. Chapter Overview

The second study strictly focused on flow around the left atrial appendage, and was designed to research how atrial fibrillation conditions changed the flow field inside the simple square channel and rectangular cavity model as well as an *in vitro* 3D silicone left heart model. Measurements were gathered using 2D PIV and 3D Tomographic PIV for the simplified model and 3D model, respectively, while investigating three Womersley number conditions over the range of Womersley numbers found in the heart. The impacts of atrial fibrillation conditions on sidewall cavities are investigated. Our results quantify the phase-to-phase changes of the flow fields and indicate that compared with the "single-peak" AFib waveform, the "double-peak" waveform of the normal health LA helps maintain the momentum of the vortical flow and reduce flow stasis inside LAA cavity throughout the cardiac cycle. Flow velocity was also seen to be much lower deep within the side wall cavities in both the *in vitro* 3D model and the 2D simplified rectangular cavity model in the normal case. These results emphasize the importance of high pulsatility in the left atrium for reducing blood flow stagnation within the left atrium appendage cavity.

3.2. Materials and Methods

3.2.1. The Pulsatile Flow Simulator and Models

The same closed loop cardiovascular flow simulator as seen in section 2.2.1 (Figure 8) was used again here. The flow rate and frequency of the flow was set to provide appropriate Reynolds and Womersley numbers for the dynamic similarity of the left atrial flow. The square channel with rectangular sidewall cavity model was again used for the first part of this experiment. The second

part utilized a 1:1 silicone left heart model as seen in Figure 16. The plane to be investigated is shown in the middle picture of this figure, with the LAA clearly marked.

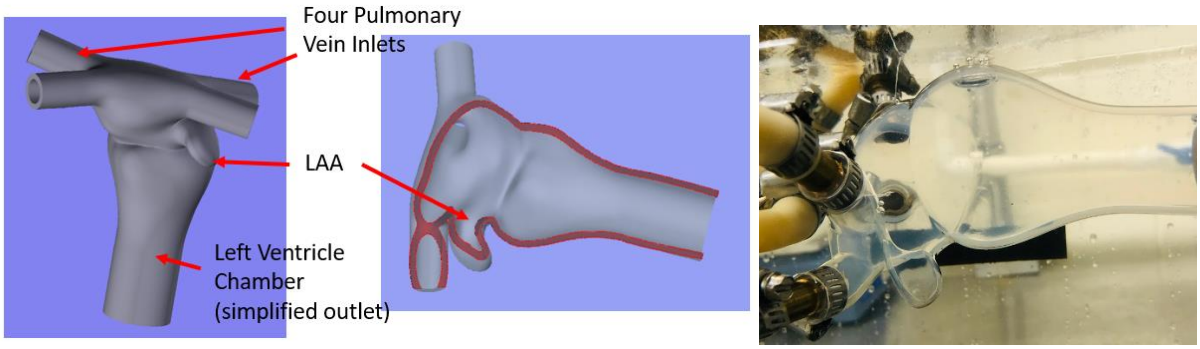

Figure 16. Model of the LA and LAA (3D CAD View Alongside an Actual Model View)

3.2.2. Waveform Models

To generate a realistic waveform for the left atrial flow, a lumped-parameter numerical model was utilized, and the results of the simulation were compared with those obtained from clinical research literatures. The computer model was modified from an open-source program, CVSim, which is a closed-loop, lumped parameter model based on an electrical-circuit analogy. The model has 21 Windkessel compartments representing the major functioning organs inside the human cardiovascular system, including four chambers of the heart (Figure 17 below). Mathematically, the dynamical system is expressed as a system of 21 ordinary differential equations with set-point baroreflex feedback controls and is solved using the 4th-order RungeKutta method in time domain. More details regarding the numerical model can be found in [72], [73]. The simulated waveform and its comparison with clinically obtained waveforms are compared in the Figure 17. The results show that our simulation results closely matched the major characteristics of the LA flow waveform.

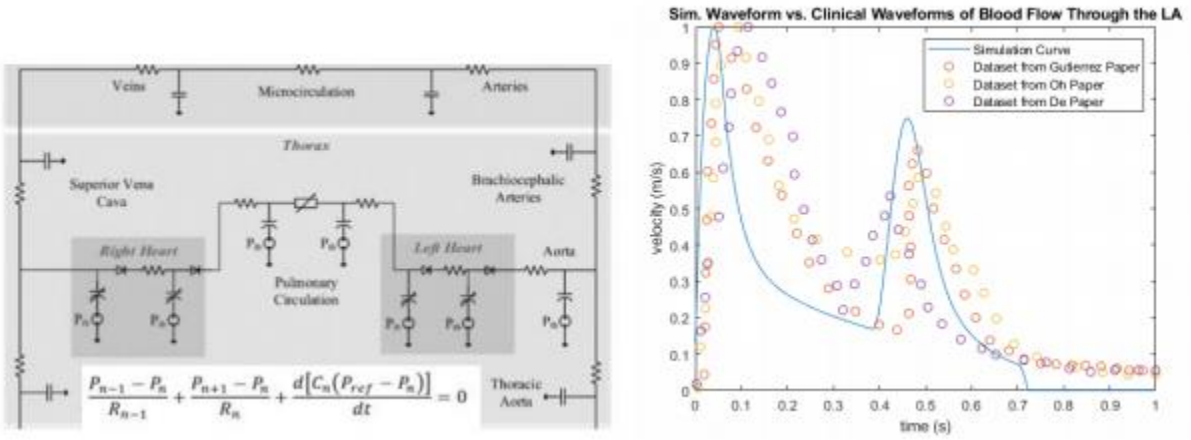

Figure 17. CVSim Model (left), and the Simulated LA Waveform Compared with Clinically Obtained Waveforms (right) [74]-[76]

It is important to characterize the differences between regular heartbeat and AFib heartbeat. This is also commonly done using echocardiography, which can be used to determine the velocity of blood ejected from the heart with respect to time. In a healthy individual, this produces a double peak waveform that represents the ratio of peak blood flow from left ventricle relaxation, known as the E wave, to peak flow from atrial contraction, known as the A wave [76]. Since the A wave is dependent on atrial contraction, individuals who experience AFib lack any type of second peak and results in a reduced blood flow through the heart [49]. Examples of regular and AFib doppler echocardiogram waveforms can be seen in Figure 18.

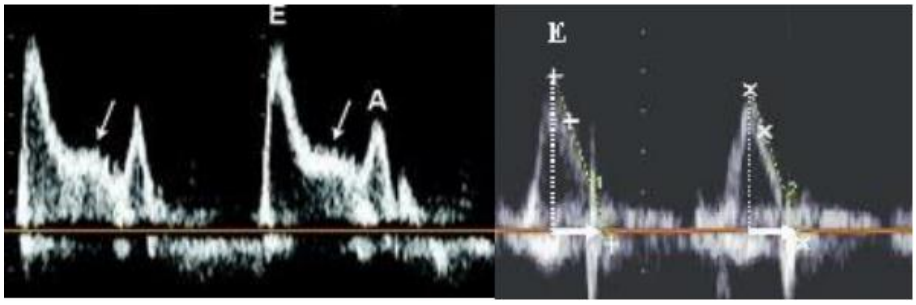

Figure 18. Clinical Doppler Echocardiogram Waveforms of a Healthy Individual (Left) and an Individual Experiencing Atrial Fibrillation (Right) [74, 77]. Note the Loss of the A Wave in the Right Image

Using this information, the previously obtained simulated LA waveform could then be modified into a waveform that matches clinical Afib waveforms. This was done by "chopping" off the A-wave of the simulation waveform, as seen in Figure 19.

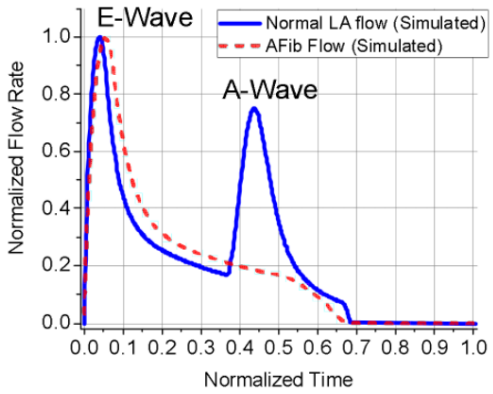

Figure 19. A Comparison of the Two Generated Simulation Waves

Again, the Womersley number is investigated for these cases. When looking at the left atrium specifically, the Womersley number varies depending on which reference length is chosen, however it varies between 10-20. Therefore, three cases were investigated, ranging from Womersley numbers of 10.2-17.7. Figure 20 compares the normalized flow rate of the input wave of the pump for both normal and atrial fibrillation conditions with the measured centerline velocity using the three different Womersley numbers used in this study.

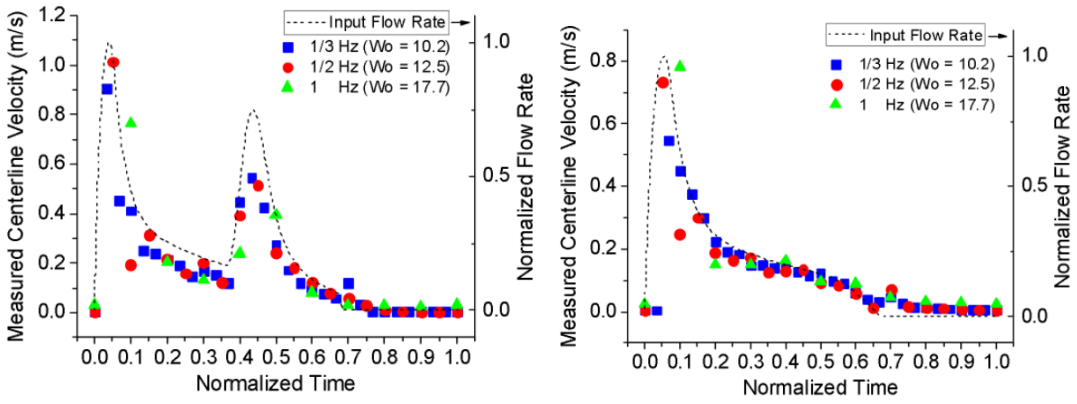

Figure 20. Comparison of the Flow Rate of the Input Waves to the Measured Centerline Velocities of Three different Womersley Numbers for the Normal Waveform (left) and the AFib Waveform (right)

3.2.3. 2D Particle Image Velocimetry

When using the square channel and rectangular cavity model, the same PIV set up as stated in section 2.2.4 and Figure 12 was used here for the 2D planar PIV measurements with the simplified model, following rules for LAA flow conditions, to quantify the flow characteristics in this model.

3.2.4. 3D Tomographic Particle Image Velocimetry

For the case of the 3D silicone left heart model, Tomographic Particle Image Velocimetry was used to quantify the flow characteristics. Tomographic PIV differs from regular PIV in that it enables the instantaneous measurement of all three velocity components in a complete 3D measurement volume.

The tomo-PIV setup used the same double-pulsed Nd:YAG laser (NewWave Gemini 200, 100mJ, 532nm) as the previous experiment. A set of concave and cylindrical lenses were applied to convert the laser beams into planes with a thickness of approximately 1cm, with this being one of the two main differences between the types of PIV. The other main difference being the usage of four 2M-pixel CCD (charge-coupled device) cameras that were placed around the test section, and the lasers and camera were synchronized by a delay generator (BNC Model 577, Berkeley Nucleonic Corp.), which was externally triggered by the pump digital output signal. Postprocessing was completed using LaVision DaVis PIV software. An illustration of the Tomographic PIV setup can be seen in Figure 21.

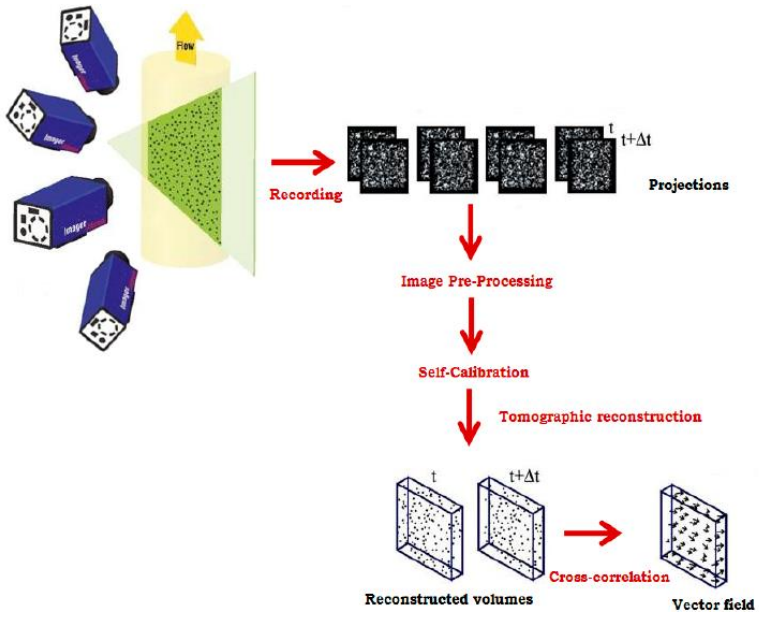

Figure 21. Tomographic Particle Image Velocimetry

To eliminate optical distortions with the silicone 3D model, refractive index matching was used. The refractive index was 1.43 and the matching was completed using a 40-60 water-glycerin mixture. An image of the model after refractive index matching can be seen at the bottom, here it is obvious that the model is very easy to see through, and near invisible for the camera. The refractive index matching can be seen in Figure 16. The system was then seeded with 50 μm glass microspheres so that the laser could be used to reflect off the microspheres and their direction and velocity could be tracked over time by the camera.

3.3. Results and Discussion

3.3.1. Atrial Fibrillation Flow in the Simplified Rectangular Model

Within the simple square channel with rectangular cavity model, when compared with the regular rhythm “double peak” mitral flow, AFib-induced mitral flow waveform significantly reduces the vortex momentum inside the “appendage” cavity, particularly towards the end of the ventricular diastole phase. This can be seen in Figure 22 where images (b-d) show an increased vortex strength due to the presence of the A wave in the normal conditions compared to the same

timeframes in the AFib conditions. In images (e-g), there is a significantly lower vortex strength presence, especially towards the end of the cycle (image g vs image d).

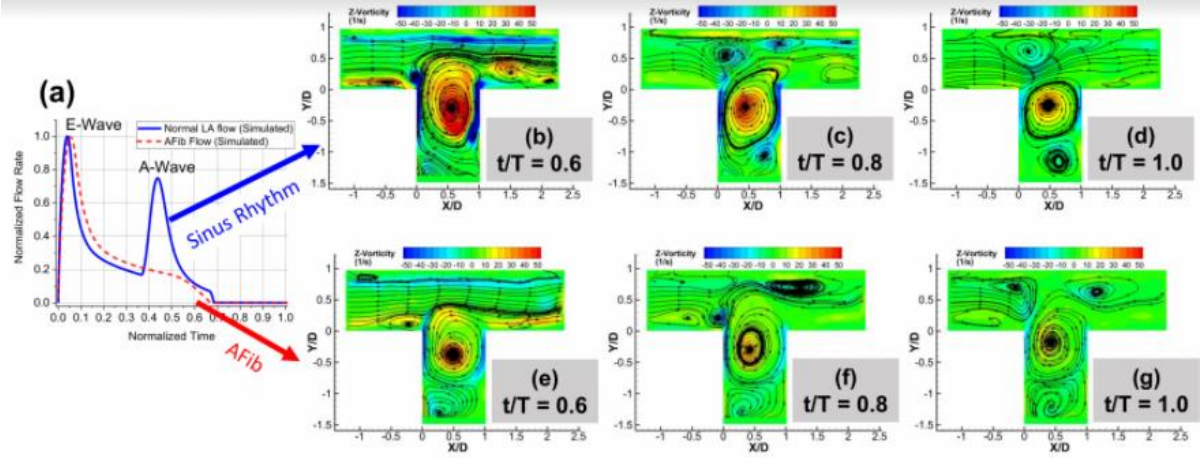

Figure 22. Flow Structures in the Rectangular Cavity Under Normal and AFib Conditions

This results in a significantly decreased flow velocity in the deep cavity that favors blood stasis which can be seen in the graph in Figure 23. These graphs show the mean velocity of blood vs time over one cycle of both the normal and AFib conditions. Each graph shows a different cavity orifice depth. With the cavity being a total of 1.5” deep, the first graph is right at the orifice, the second is 0.5” into the cavity, and the third is 1.0” into the cavity. It is obvious from these graphs that the flow velocity is much lower deeper in the cavity. As well, the peak seen around T/t = 0.5-0.6 where the A Wave occurs under normal flow is not seen in the AFib flow, and results in a much lower velocity at those time steps in every case. This flow stagnation is the mechanism which leads to the formation of blood clots inside side wall cavities.

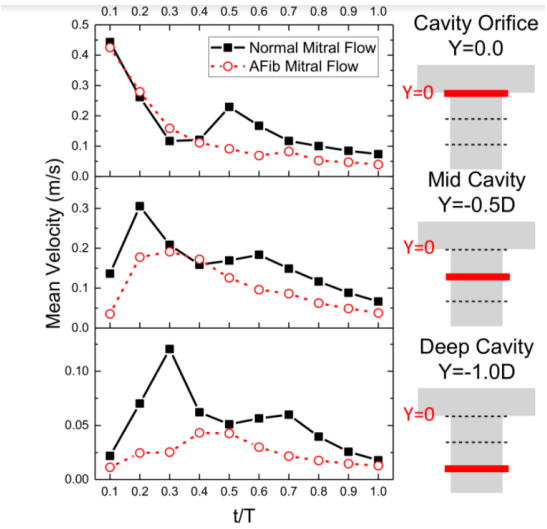

Figure 23. In-Cavity Flow Velocity Under Normal and AFib Conditions

3.3.2. Atrial Fibrillation Flow in the Silicone Left Heart Model

Similar results can be found when looking at the left atrial appendage in the 1:1 3D silicone left heart model. Figure 24 shows the instantaneous 3D vorticity fields show highly turbulent flow structures throughout the fluid transport cycle. As well, in the regular LA flow, high vorticity structures are still observed in the LAA at 43% of the cycle (caused by atrial pumping – 2nd peak/A wave). That is compared to AFib flow, where the flow dissipates fast and less vorticity is observed in the LAA after 43% of the cycle, due to the lack of the 2nd peak.

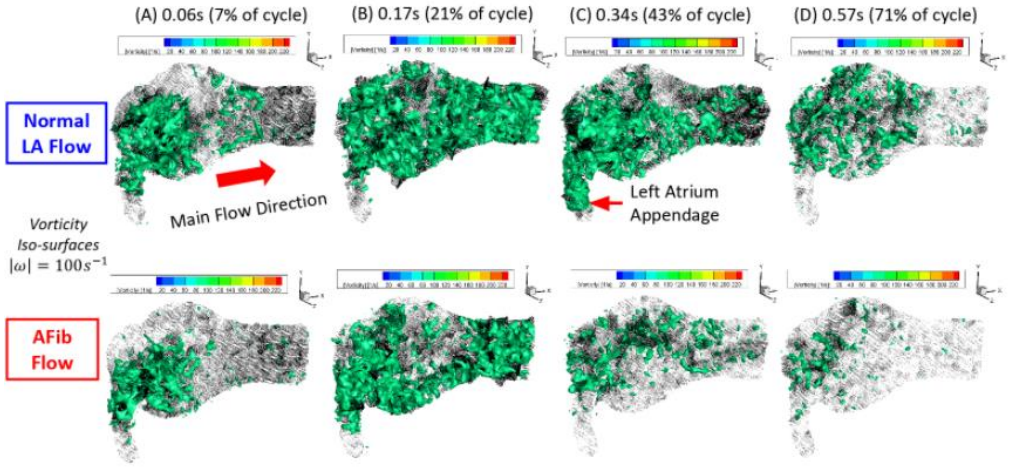

Figure 24. Flow Structures in the 3D Silicone Model Under Normal and AFib Conditions

And again, similarly to the simple square channel with rectangular cavity model, velocity profiles at different phases within the 3D silicone left heart model were also analyzed. Flow velocity was analyzed over 100 frames, and as shown in Figure 25, the average velocity magnitude within the normal LA flow is shown to be much higher compared to the AFib flow, especially much later through the cycle. Again, this is due to the lack of the second peak/A wave. This reduction in blood flow velocity would result in blood flow stagnation which would increase the likelihood of blood clot formation.

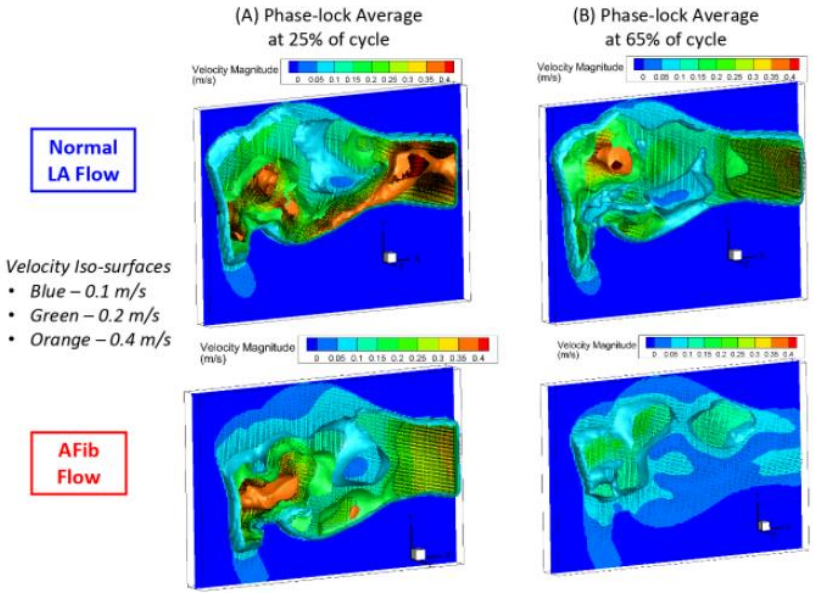

Figure 25. Average Velocity Magnitude Iso-Surfaces at Early and Late Cycle Times in the Silicone Model

3.4. Conclusions

An experimental study of pulsatile flow with normal and atrial fibrillation conditions was performed for both a simple square channel with rectangular cavity model as well as a 1:1 3D silicone left heart model. The results indicate that compared with the "single-peak" AFib waveform, the "double-peak" waveform of the normal health LA helps maintain the momentum of the vortical flow and reduce flow stasis inside LAA cavity throughout the cardiac cycle. As

well, flow stasis inside the LAA is believed to be one of the major causes of AFib-induced stroke, and the results of the study emphasize the important role of high pulsatility of the main LA flow in determining the flow momentum inside the cavity. This means that enhancing the flow inside the LAA cavity during AFib could potentially reduce the risks of flow stasis and thrombi formation.

CHAPTER 4. STUDY OF SLIPS SURFACE AND ITS EFFECT ON PULSATILE FLOW IN THE SIDE WALL CAVITY MODEL IN ATRIAL FIBRILLATION CONDITIONS

4.1. Chapter Overview

This study was designed to research how a unique slippery surface could be used on the inner walls of a cavity model to enhance the flow and prevent flow stagnation discussed in Chapter 3. Measurements were gathered using 2D PIV with the simplified model while investigating three Womersley number conditions. The impacts of a SLIPS surface inserted on three walls of the simplified rectangular cavity model. This experiment was necessary because it could provide useful insight to stopping flow stagnation within biological side wall cavity models without outright blocking the cavity itself. This is most useful in the case of the LAA, where normal treatment of AFib caused blood clots in the LAA involves simply closing it off from the rest of the heart. The results show that a SLIPS surface, particularly on the rear side of the cavity, is helpful to reduce the wall shear and to allow the vortical flow to reach deeper towards the bottom of the cavity.

4.2. Materials and Methods

4.2.1. The Pulsatile Flow Simulator and Cavity Model

The same closed loop cardiovascular flow simulator as seen in section 3.2.1 (Figure 8) was used again here. The flow rate and frequency of the flow was set to provide appropriate Reynolds and Womersley numbers for the dynamic similarity of the left atrial flow. The square channel with rectangular sidewall cavity model was again used for the first part of this experiment. The only difference is that the two side walls, and lower wall of the cavity were covered in the SLIPS surface. Those walls are marked in Figure 26.

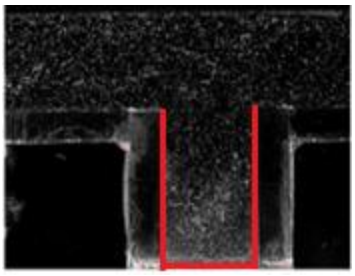

Figure 26. Simple Cavity Model with the SLIPS Surface Walls Marked by Red Lines

4.2.2. SLIPS Surface

The novel self-healing, slippery liquid-infused porous surface (SLIPS) was developed by the Wong Laboratory for Nature Inspired Engineering at Pennsylvania State University. This surface utilizes the liquid-repelling microtextured surfaces of other hydrophobic and superhydrophobic surfaces while also being lubricated by a fluid that repels many other fluids. This kind of surface can be very useful as it can withstand pressures inside a flow field while also maintaining a fluid-fluid boundary between water and the surface of SLIPS, even under flow [64]. Figure 7 depicts the SLIPS surface. As well, the SLIPS surface is naturally hydrophobic, even after prolonged static immersion, as seen in Figure 27.

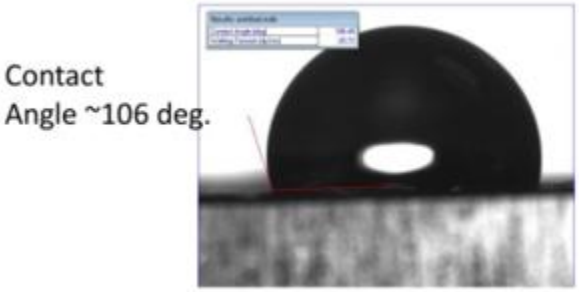

Figure 27. SLIPS Surface Exhibiting Hydrophobicity

However, verification of the ability for the infused fluid to maintain stability even under flow needed to be verified. This was done by running a 12 in. strip of the SLIPS surface inside the closed loop cardiovascular flow simulator seen in section 3.2.1 (Figure 8) for times of 5, 10, 15, 20, 30, 40, 50 and 60 minutes. The flow conditions were the built-in programmable waveform of

the pulsatile flow pump through a user-defined skewed sinusoidal function as described in section 3.2.2 at a volumetric flow rate of 5L/min. At each of those times, the surface was removed and placed on an inclined surface where velocity measurements of water droplets flowing down the surface were gathered. For each timestep, 10 velocity measurements were gathered and averaged and compared to velocity measurements of droplets flowing down the same kind of silicone used in the 1:1 3D left heart model.

4.2.3. Waveform Models

This study utilized the same normal and atrial fibrillation waveforms as seen in the previous chapter. These waveforms can be seen in Figures 17-19 in Section 3.2.2 and followed all conditions discussed in that section.

4.2.4. Particle Image Velocimetry

Since this experiment only used the square channel with a rectangular cavity model, the same PIV set up as stated in Section 2.2.4 and Figure 12 was repeated, following rules for LAA flow conditions, to quantify the flow characteristics in this model.

4.3. Results and Discussion

4.3.1. SLIPS Surface Verification Under Flow

First, the SLIPS surface had to be verified that it did not break down under pulsatile flow. This was done by immersing the surface under flow for various timesteps and then measuring the velocity of a water droplet as it flows down the surface set at an incline. The average velocity of droplets stayed near constant no matter how long the surface was under flow, with an average velocity of 2.09m/s for no time under flow and 2.07m/s after an hour in the closed loop cardiovascular flow simulator. This means that the infused fluid would not break down under our flow conditions for extended periods of time. Meanwhile, droplets flowing down the silicone

surface had a velocity 0.627m/s. Results comparing the silicone with the SLIPS surface after being immersed for a 0, 10, and 60 minutes can be seen in Figure 28. The rest of the results can be seen in Table 3 below. This means that the SLIPS surface increased the velocity on average by 3.33 times. With this completed, the SLIPS surface was then deemed usable within the model without risk of breakdown of the surface itself. Figure 29 shows a water droplet flowing down the SLIPS surface at two different frames, the first being just before the timer starts, and the next being just before it ends.

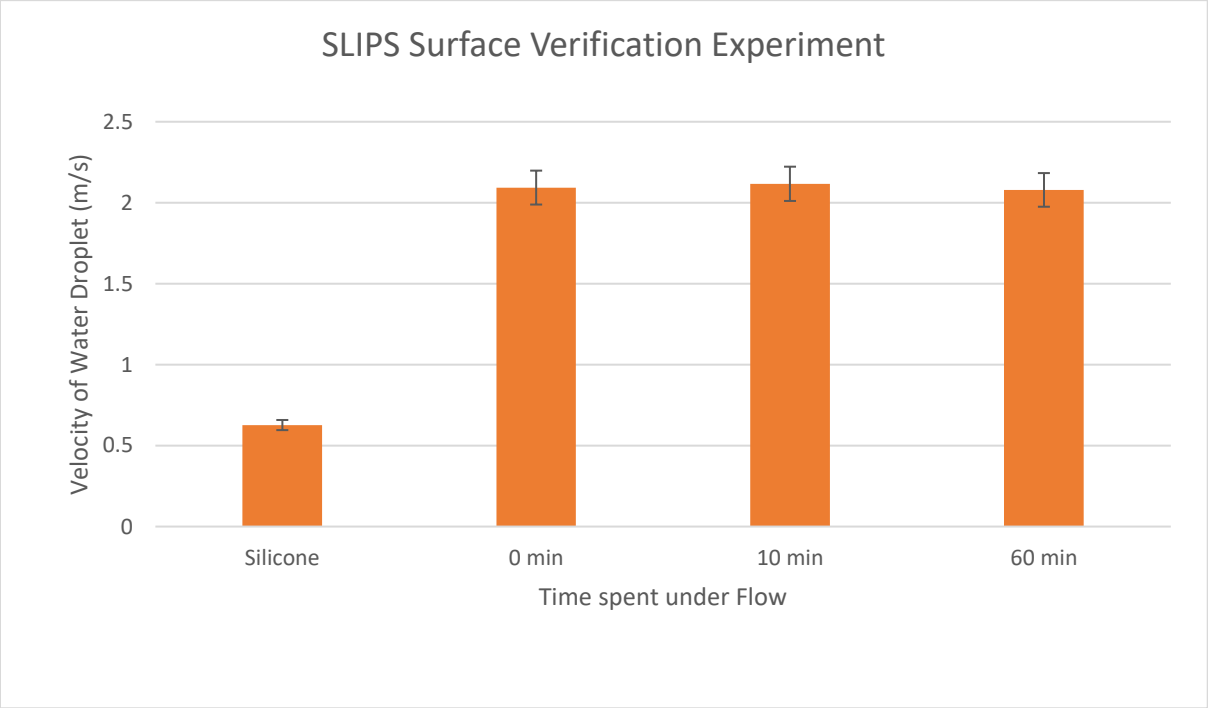

Figure 28. Results of the SLIPS Surface Verification Experiment

Table 3. Slippery Surface Verification Results

	Silicone	**0min**	**5min**	**10min**	**15min**	**20min**	**25min**	**30min**	**40min**	**50min**	**60min**
Avg t 6"	0.2431	0.0728	0.075	0.072	0.0728	0.0717	0.072	0.0743	0.0726	0.0722	0.0733
V (in/s)	24.68120	82.41758	80	83.33333	82.41758	83.68200	83.33333	80.75370	82.64463	83.10249	81.85538
V (m/s)	0.62690	2.09341	2.03200	2.11667	2.09341	2.12552	2.11667	2.05114	2.09917	2.11080	2.07913103

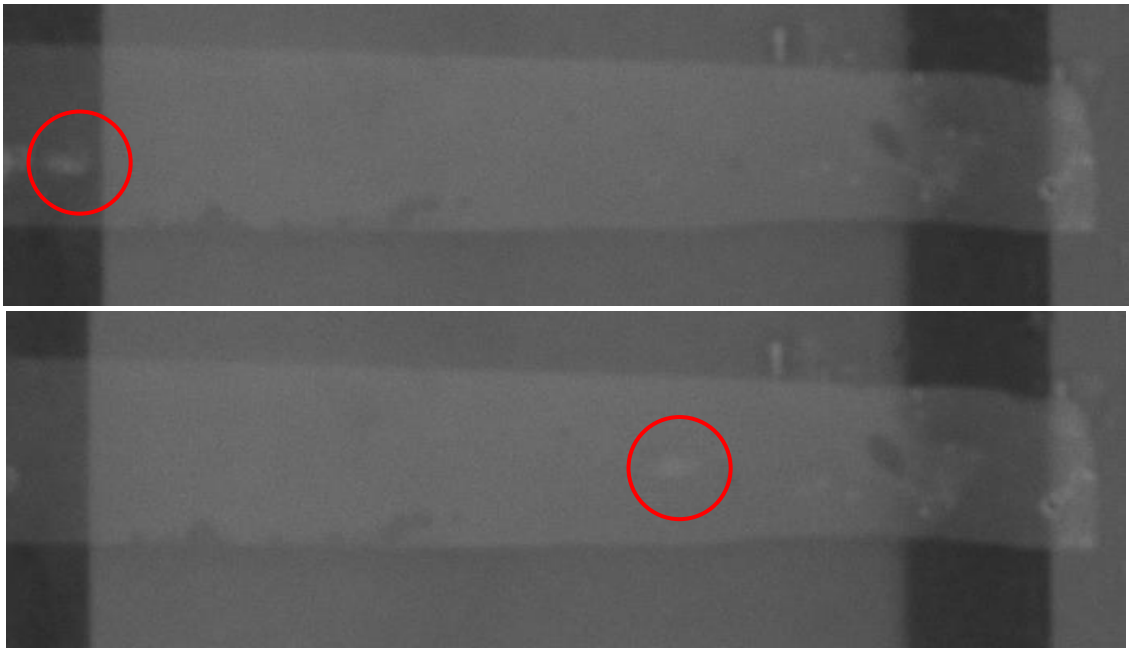

Figure 29. Water Droplet Flowing Down the SLIPS Surface After Immersion

4.3.2. Effects of the SLIPS Surface Insert

Results of gathering pulsatile flow velocity data in the simple cavity model with the slips surface are shown in Figure 30, with this being the lowest Womersley number case. Results from without the SLIPS surface are shown on top with the SLIPS surface shown on bottom. These images again show out-of-plane vorticity contours with velocity vectors throughout the cycle (10%-60%). From these graphs, it is obvious that when comparing velocity vectors and vorticity fields, vorticity difference and shear stress, especially on the right side of the cavity is much lower when the SLIPS surface is present. This is especially obvious at the 10 and 15% of cycle cases where the amount of "blue" is lower in the cases with the SLIPS surface present. It should also be noted that because of the SLIPS surface, flow seems to go deeper into the cavity. This observation is most noticeable in the last two sets of images for these results

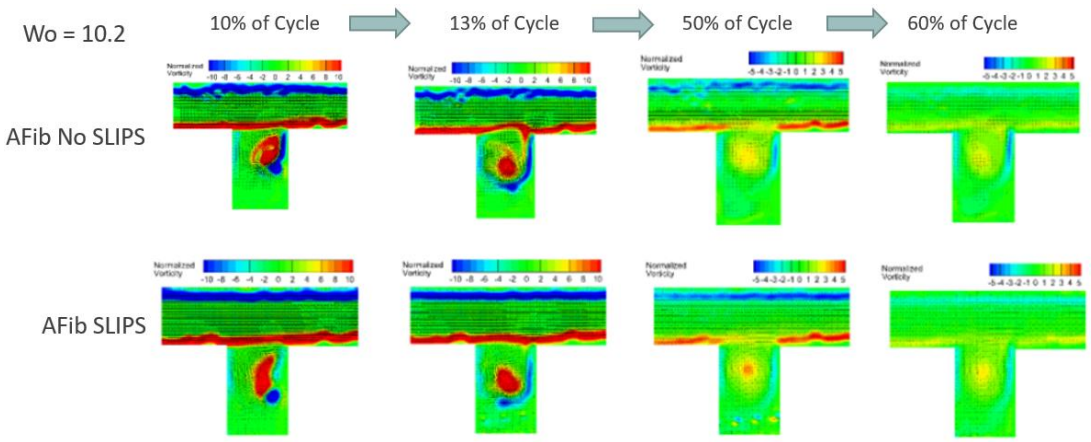

Figure 30. Velocity Vectors and Out-of-Plane Vorticity Fields of Pulsatile Flow Comparing the AFib Case with and without the SLIPS Surface Present at Wo=10.2

Figure 31 shows velocity vectors and out-of-plane vorticity fields of pulsatile flow comparing the AFib case with and without the SLIPS surface present as well. Looking at the next higher Womersley number case, Wo = 12.5, meaning that this flow has higher frequency than the one before it, it shows the same lower vorticity on the back side of the model, however the change is less significant here. This difference is most noticeable in the first three sets of images again. The same observation can be made about the flow going deeper into the cavity as well. This is most noticeable in the last set of images for this set of results.

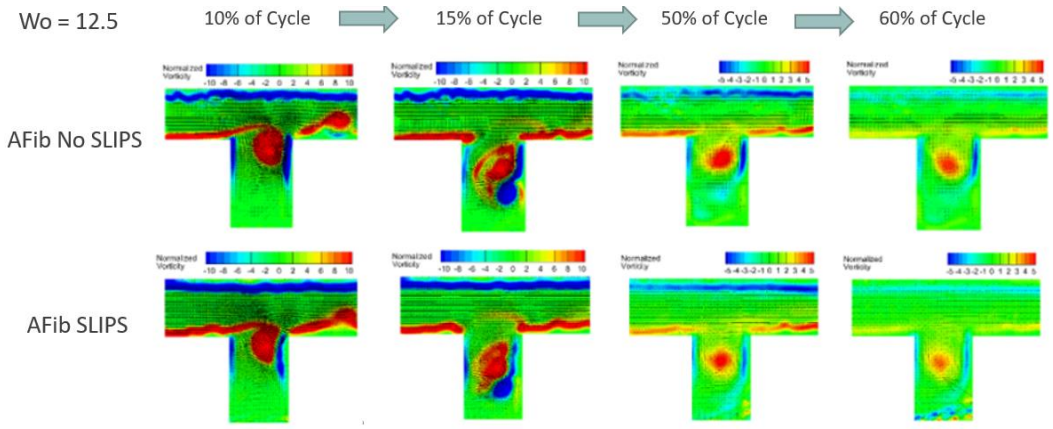

Figure 31. Velocity Vectors and Out-of-Plane Vorticity Fields of Pulsatile Flow Comparing the AFib Case with and without the SLIPS Surface Present at Wo=12.5

Finally, Figure 32 shows the same kind of data as Figures 30-31, but with the highest Womersley number case at Wo=17.7. Again, this just means that the frequency of the pulsatile flow has increased. This case shows not as much difference between the images with the SLIPS surface compared to the ones without. This could indicate that the SLIPS surface is more effective under lower frequency pulsatile flow conditions rather than higher frequency conditions.

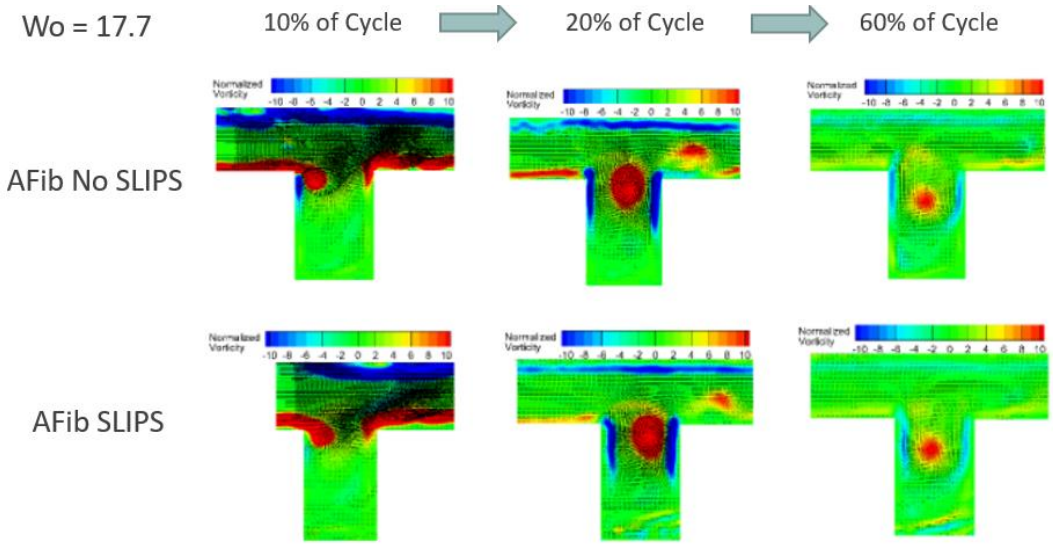

Figure 32. Velocity Vectors and Out-of-Plane Vorticity Fields of Pulsatile Flow Comparing the AFib Case with and without the SLIPS Surface Present at Wo=17.7

4.4. Conclusions

Overall, looking at these images of velocity vectors and vorticity fields for pulsatile flow past the simple cavity under normal left atrial and AFib flow with and without inserted SLIPS surfaces, the comparison does show a notable difference in vorticity and shear stress, especially along the backside of the cavity in the first three sets of images. This results in vortical flow being able to reach lower into the cavity when the SLIPS surface is present. However, this trend is not as noticeable as Womersley number increases. In conclusion, the results from these chapters indicate that the double peaked normal waveform helps maintain the momentum of vortical flow and reduces flow stasis inside the left atrial appendage throughout the cardiac cycle. And since

flow stasis is believed to be one of the major causes of AFib induced stroke, this puts an emphasis on the importance of high pulsatility of the main left atrial flow in determining the flow momentum inside the cavity. As well, it shows that a SLIPS surface, particularly on the rear side of the cavity, is helpful to reduce the wall shear and to allow the vortical flow to reach deeper towards the bottom of the cavity.

CHAPTER 5. CONCLUSIONS AND FUTURE WORK

To summarize the conclusions, Chapter 2 concluded that the presence of the mesh diverted the main flow and prohibited the formation of the primary vortices. With mesh implanted, a penetrated jet flow was developed near the front end of the cavity, and the superhydrophobic mesh significantly decreased the kinetic energy of the jet flow penetrating the simple cavity. Chapter 3 concluded that compared with the "single-peak" AFib waveform, the "double-peak" waveform of the normal health LA helps maintain the momentum of the vortical flow and reduce flow stasis inside LAA cavity throughout the cardiac cycle. And Chapter 4 shows that a SLIPS surface can be helpful to reduce the wall shear and to allow the vortical flow to reach deeper towards the bottom of the cavity when under the same conditions observed in Chapter 3.

It is important to note the limitations of this kind of experiment so that they can be discussed and improved upon for the future. One such limitation includes the use of the glycerol-water mixture in place of blood. This mixture was chosen, in part, because of its compatibility with the PIV system, but there are notable differences between it and blood. One of the major differences is that our mixture is a Newtonian fluid, while blood is a non-Newtonian fluid. This means that the viscosity of blood changes depending on how much stress is put on it while in the water-glycerol mixture, the viscosity is independent of the shear rate.

Another difference involves the silicone model: while it is geometrically similar to the left side of the heart, the silicone/acrylic used in the two models does not represent the real tissue properties seen inside blood vessels and the heart. The lining inside of the heart and blood vessels allow for exchanges between the blood stream and surrounding tissues and are also made up of biological material rather than artificial ones [78].

As well, atrial fibrillation involves the chaotic beating of heart wall tissue, which was not simulated for in these studies. While our atrial fibrillation waveform accounted for the loss of the A wave, it still beat in regular intervals, which would not be seen in clinical AFib cases. This can be observed in Figure 6 where the echocardiogram shows no rhythm to the beating.

And, the PIV measurement system was unable to measure more than a 10mm thick volume in 3D tomographic PIV. This means that the current set up does not allow for the obtaining of the entire flow field inside the silicone left heart model at one time.

The current research can be extended in a few directions in the future, which includes remedying some of the previously mentioned limitations. There are some ideas that I would have liked to try to expand on the results explained already in Chapters 2, 3, and 4. The following ideas could be used to improve upon already obtained results:

1. Even though the waveform used for AFib involved the removal of the A wave, which matches clinical representations of AFib in the heart, the waveform itself still "beat" in regular intervals. Meanwhile, while experiencing actual AFib, the heart beats sporadically with no specific rhythm. This applies to all experiments run that involve modeling the left atrium and left atrial appendage but not aneurysms.

2. The SLIPS surface could be used in a similar fashion to Chapter 4, but inside of the 1:1 3D silicone left heart model. However, fixing the surface inside of such a small area has proven difficult, as using glue, silicone, or staples to adhere the surface to the model would damage it or block the view of the cameras. As well, having the surface on the inside of the model would block the view of the cameras for gathering tomographic PIV data.

Using these ideas, the idea of using hydrophobic surfaces to improve blood flow via flow diversion or enhancement devices could be further improved upon.

REFERENCES

[1] Cardiovascular System; US National Library of Medicine; Medical Subject Headings (MeSH)

[2] Starr, Cecie; Evers, Christine; Starr, Lisa (2009). *Biology: Today and Tomorrow With Physiology*. Cengage Learning. p. 422. ISBN 978-0-495-56157-6.

[3] Baskurt, OK; Hardeman M; Rampling MW; Meiselman HJ (2007). *Handbook of Hemorheology and Hemodynamics. Biomedical and Health Research*. Amsterdam, Netherlands: IOS Press. pp. 455. ISBN 978-1586037710. ISSN 0929-6743.

[4] Urgo Medical, Laboratoires Urgo, http://www.urgomedical.com/

[5] R. T. Jones, "*Blood flow,"* Annual Review of Fluid Mechanics, vol. 1, no. 1, pp. 223–244, 1969.

[6] Ponzini, R. "*Womersley Number-Based Estimates of Blood Flow Rate in Doppler Analysis: In Vivo Validation by Means of Phase-Contrast MRI*" IEEE Transactions on Biomedical Engineering, VOL. 57, NO. 7, JULY 2010

[7] Doenst, T. "*Fluid-Dynamic Modeling of the Human Left Ventricle: Methodology and Application to Surgical Ventricular Reconstruction"* The Society of Thoracic Surgeons 2009 doi:10.1016/j.athoracsur.2009.01.036

[8] Dusenbery, David B. (2009*). Living at Micro Scale*. Cambridge, Massachusetts: Harvard University Press. ISBN 9780674031166.

[9] Hoi, Y., Woodward, S. H., Kim, M., Taulbee, D. B., and Meng, H. (June 15, 2006). *"Validation of CFD Simulations of Cerebral Aneurysms With Implication of Geometric Variations."* ASME. J Biomech Eng. December 2006; 128(6): 844–851. https://doi.org/10.1115/1.2354209

[10] Moore, J. E. et. al. *Hemodynamics in the abdominal aorta: a comparison of in vitro and in vivo measurements*. Journal of Applied Physiology April 1994. https://doi.org/10.1152/jappl.1994.76.4.1520

[11] "*Aneurysms*". Society of NeuroInterventional Surgery.

[12] Nabong, Jennica Rica; David, Guido (October 2017). *"Finite element model of size, shape and blood pressure on rupture of intracranial saccular aneurysms"*. Journal of Physics: Conference Series. 893: 012054. doi:10.1088/1742-6596/893/1/012054. ISSN 1742-6596.

[13] Algabri, Y. A.; Rookkapan, S.; Chatpun, S. (September 2017). *"Three-dimensional finite volume modelling of blood flow in simulated angular neck abdominal aortic aneurysm"*. IOP Conference Series: Materials Science and Engineering. 243: 012003. doi:10.1088/1757-899X/243/1/012003. ISSN 1757-899X.

[14] Sarrami-Foroushani, Ali; Lassila, Toni; Hejazi, Seyed Mostafa; Nagaraja, Sanjoy; Bacon, Andrew; Frangi, Alejandro F. (2019-06-25). *"A computational model for prediction of clot platelet content in flow-diverted intracranial aneurysms"*. Journal of Biomechanics. **91**: 7–13. doi:10.1016/j.jbiomech.2019.04.045. ISSN 0021-9290. PMID 31104921.

[15] Brain Aneurysm Foundation, Hanover, MA, https://bafound.org/

[16] L. Pierot, *"Flow diverter stents in the treatment of intracranial aneurysms: Where are we?,"* J. Neuroradiol., 7 © 2020 by ASME vol. 38, no. 1, pp. 40–46, Mar. 2011, doi: 10.1016/j.neurad.2010.12.002.

[17] P. I. D'Urso, G. Lanzino, H. J. Cloft, and D. F. Kallmes, *"Flow Diversion for Intracranial Aneurysms,"* Stroke, Aug. 2011.

[18] D. F. Kallmes, Y. H. Ding, D. Dai, R. Kadirvel, D. A. Lewis, and H. J. Cloft, *"A New Endoluminal, Flow- Disrupting Device for Treatment of Saccular Aneurysms,"* Stroke, Aug. 2007.

[19] R. Dholakia, C. Sadasivan, D. J. Fiorella, H. H. Woo, and B. B. Lieber, *"Hemodynamics of Flow Diverters,"* J. Biomech. Eng., vol. 139, no. 2, pp. 021002-021002–10, Jan. 2017, doi: 10.1115/1.4034932.

[20] C. Groden, J. Laudan, S. Gatchell, and H. Zeumer, *"Three-Dimensional Pulsatile Flow Simulation before and after Endovascular Coil Embolization of a Terminal Cerebral Aneurysm,"* J. Cereb. Blood Flow Metab., vol. 21, no. 12, pp. 1464–1471, Dec. 2001, doi: 10.1097/00004647-200112000-00011.

[21] B. B. Lieber, A. P. Stancampiano, and A. K. Wakhloo, *"Alteration of hemodynamics in aneurysm models by stenting: influence of stent porosity,"* Ann. Biomed. Eng., vol. 25, no. 3, pp. 460–469, Jun. 1997.

[22] B. B. Lieber, V. Livescu, L. N. Hopkins, and A. K. Wakhloo, *"Particle Image Velocimetry Assessment of Stent Design Influence on Intra-Aneurysmal Flow,"* Ann. Biomed. Eng., vol. 30, no. 6, pp. 768–777, Jun. 2002, doi: 10.1114/1.1495867.

[23] A. L. Trager, C. Sadasivan, J. Seong, and B. B. Lieber, *"Correlation between angiographic and particle image velocimetry quantifications of flow diverters in an in vitro model of elastase-induced rabbit aneurysms,"* J. Biomech. Eng., vol. 131, no. 3, p. 034506, Mar. 2009, doi: 10.1115/1.3049528.

[24] B. Lubicz et al., *"Flow-Diverter Stent for the Endovascular Treatment of Intracranial Aneurysms,"* Stroke, Oct. 2010.

[25] G. K. C. Wong, M. C. L. Kwan, R. Y. T. Ng, S. C. H. Yu, and W. S. Poon, *"Flow diverters for treatment of intracranial aneurysms: Current status and ongoing clinical trials,"* J. Clin. Neurosci., vol. 18, no. 6, pp. 737–740, Jun. 2011, doi: 10.1016/j.jocn.2010.10.011.

[26] S. O. Kim, Y. G. Chung, Y. S. Won, and M. H. Rho, *"Delayed Ischemic Stroke after Flow Diversion of Large Posterior Communicating Artery Aneurysm*," J. Cerebrovasc. Endovasc. Neurosurg., vol. 18, no. 1, pp. 19–26, Mar. 2016, doi: 10.7461/jcen.2016.18.1.19.

[27] J. R. Cebral et al., *"Aneurysm Rupture Following Treatment with Flow-Diverting Stents: Computational Hemodynamics Analysis of Treatment,"* Am. J. Neuroradiol., vol. 32, no. 1, pp. 27–33, Jan. 2011, doi: 10.3174/ajnr.A2398.

[28] P. Boillot et al., *"Multi-time lag PIV analysis of steady and pulsatile flows in a sidewall aneurysm,"* Interventional Neuroradiology Unit, University Hospitals of Geneva, January 2014

[29] Ford, M. D., Nikolov, H. N., Milner, J. S., Lownie, S. P., DeMont, E. M., Kalata, W., Loth, F., Holdsworth, D. W., and Steinman, D. A. (April 3, 2008). *"PIV-Measured Versus CFD-Predicted Flow Dynamics in Anatomically Realistic Cerebral Aneurysm Models."* ASME. *J Biomech Eng*. April 2008; 130(2): 021015. https://doi.org/10.1115/1.2900724

[30] Le, T.B., Troolin, D.R., Amatya, D. *et al. "Vortex Phenomena in Sidewall Aneurysm Hemodynamics: Experiment and Numerical Simulation." Ann Biomed Eng* 41, 2157–2170 (2013). https://doi.org/10.1007/s10439-013-0811-9

[31] Ugron, Á., Farinas, MI., Kiss, L. *et al. "Unsteady velocity measurements in a realistic intracranial aneurysm model." Exp Fluids* 52, 37–52 (2012). https://doi.org/10.1007/s00348-011-1206-z

[32] Le T.B., Eidenschink E., Drofa A. (2020) *"Impacts of Flow Diverters on Hemodynamics of Intracranial Aneurysms".* In: Ateshian G., Myers K., Tavares J. (eds) Computer Methods, Imaging and Visualization in Biomechanics and Biomedical Engineering. CMBBE 2019. Lecture Notes in Computational Vision and Biomechanics, vol 36. Springer, Cham. https://doi.org/10.1007/978-3-030-43195-2_2

[33] Y. Zhang, W. Chong, Y. Qian, *"Investigation of intracranial aneurysm hemodynamics following flow diverter stent treatment,"* Medical Engineering & Physics,Volume 35, Issue 5,2013,Pages 608-615,ISSN 1350-4533,https://doi.org/10.1016/j.medengphy.2012.07.005.

[34] Yujie Li, David I. Verrelli, William Yang, Yi Qian, Winston Chong, *"A pilot validation of CFD model results against PIV observations of haemodynamics in intracranial aneurysms treated with flow-diverting stents,"* Journal of Biomechanics, Volume 100, 2020, 109590, ISSN 0021-9290, https://doi.org/10.1016/j.jbiomech.2019.109590.

[35] Clauser, J., Knieps, M.S., Büsen, M. *et al.* A Novel Plasma-Based Fluid for Particle Image Velocimetry (PIV): *In-Vitro* Feasibility Study of Flow Diverter Effects in Aneurysm Model. *Ann Biomed Eng* 46, 841–848 (2018). https://doi.org/10.1007/s10439-018-2002-1

[36] X. Hou et al., *"Preparation of polypropylene superhydrophobic surface and its blood compatibility,"* Colloids Surf. B Biointerfaces, vol. 80, no. 2, pp. 247–250, Oct. 2010, doi: 10.1016/j.colsurfb.2010.06.013.

[37] S. Hoshian, E. Kankuri, R. H. A. Ras, S. Franssila, and V. Jokinen, *"Water and Blood Repellent Flexible Tubes,"* Sci. Rep., vol. 7, no. 1, p. 16019, Nov. 2017, doi: 10.1038/s41598-017-16369-3.

[38] Wang, Shutao; Jiang, L. (2007). *"Definition of superhydrophobic states".* Advanced Materials. 19 (21): 3423–3424. doi:10.1002/adma.200700934

[39] Hensel, R., Neinhuis, C., Werner, C., "*The springtail cuticle as a blueprint for omniphobic surfaces,"* Royal Society of Chemistry, *Chem. Soc. Rev.*, 2016, **45**, 323-341, DOI: 10.1039/C5CS00438A

[40] D. R. Schmidt, H. Waldeck, and W. J. Kao, *"Protein Adsorption to Biomaterials,"* in Biological Interactions on Materials Surfaces, Springer, New York, NY, 2009, pp. 1–18.

[41] A. Vaterrodt, B. Thallinger, K. Daumann, D. Koch, G. M. Guebitz, and M. Ulbricht, *"Antifouling and Antibacterial Multifunctional Polyzwitterion/Enzyme Coating on Silicone*

Catheter Material Prepared by Electrostatic Layer-by-Layer Assembly," Langmuir, vol. 32, no. 5, pp. 1347–1359, Feb. 2016, doi: 10.1021/acs.langmuir.5b04303.

[42] J. Zhao, L. Song, J. Yin, and W. Ming, *"Anti-bioadhesion on hierarchically structured, superhydrophobic surfaces,"* Chem. Commun., vol. 49, no. 80, pp. 9191–9193, 2013, doi: 10.1039/C3CC44971H.

[43] E. Gogolides, K. Ellinas, and A. Tserepi, *"Hierarchical micro and nano structured, hydrophilic, superhydrophobic and superoleophobic surfaces incorporated in microfluidics, microarrays and lab on chip microsystems,"* Microelectron. Eng., vol. 132, pp. 135–155, Jan. 2015, doi: 10.1016/j.mee.2014.10.002.

[44] J. B. Wolinsky, Y. L. Colson, and M. W. Grinstaff, *"Local drug delivery strategies for cancer treatment: Gels, nanoparticles, polymeric films, rods, and wafers,"* J. Controlled Release, vol. 159, no. 1, pp. 14–26, Apr. 2012, doi: 10.1016/j.jconrel.2011.11.031.

[45] D. L. Bark et al., "*Hemodynamic Performance and Thrombogenic Properties of a Superhydrophobic Bileaflet Mechanical Heart Valve,"* Ann. Biomed. Eng., vol. 45, no. 2, pp. 452–463, Feb. 2017, doi: 10.1007/s10439-016-1618-2.

[46] Peter Lin, Chii-Wann Lin, Raafat Mansour, Frank Gu, "*Improving biocompatibility by surface modification techniques on implantable bioelectronics,"* Biosensors and Bioelectronics, Volume 47, 2013, Pages 451-460, ISSN 0956-5663, https://doi.org/10.1016/j.bios.2013.01.071.

[47] Longyue Gao, Weiqi Zhou, Yuanbo Wang, et al., "*Fabrication of hydrophobic structures on stent by direct three-beam laser interference lithography,"* Optik, Volume 127, Issue 13, 2016, Pages 5211-5214, ISSN 0030-4026, https://doi.org/10.1016/j.ijleo.2016.02.075.

[48] Wang, J., Gao, L., Li, Y. *et al. "Experimental research on laser interference micro/nano fabrication of hydrophobic modification of stent surface." Lasers Med Sci* **32,** 221–227 (2017). https://doi.org/10.1007/s10103-016-2105-6

[49] Al-Saady NM; et al. (1999). *"Left atrial appendage: structure, function, and role in thromboembolism:Review"*. Heart. 82 (5):54754. doi:10.1136/hrt.82.5.547. PMC 1760793. PMI D 10525506.

[50] Guhathakurta S, Kurian VM, Manmohan G, Cherian KM (2004). *"Mitral valve reoperation through the left atrial appendage in a patient with mesocardia"*. Tex Heart Inst J. 31 (3): 316–18. PMC 521780. PMID 15562857.

[51] *"Heart Disease Other Related Conditions*". cdc.gov. 3 September 2014. Archived from the original on 14 February 2015. Retrieved 19 February 2015.

[52] "*Atrial Fibrillation*". Centers for Disease Control and Prevention (December 2019) cdc.gov

[53] Di Biase L. *"Thrombogenic and arrhythmogenic roles of the left atrial appendage in atrial fibrillation"*. Circulation American Heart Association (October 2018), 138(18)

[54] Waks, Jonathan W; Josephson, Mark E (August 2015). *"Mechanisms of Atrial Fibrillation – Reentry, Rotors and Reality"*. Arrhythmia & Electrophysiology Review. 3 (2): 90–100. doi:10.15420/aer.2014.3.2.90. PMC 4711504. PMID 26835073

[55] Gray, Huon H.; Keith D. Dawkins; Iain A. Simpson; John M. Morgan (2002). Lecture Notes on Cardiology. Boston: Blackwell Science. p. 135. ISBN 978-0-86542-864-5.

[56] The Afib Clinic, Grandview Medical Center, Alabama Cardiovascular Group, https://www.theafibclinic.com/atrial-fibrillation/what-is-atrial-fibrillation-afib/

[57] Institute for Quality and Efficiency in Health Care (IQWiG); 2006-. *Atrial fibrillation: Does left atrial appendage closure prevent strokes?* 2017 Oct 5

[58] D. R. Holmes et al., *"Left Atrial Appendage Closure as an Alternative to Warfarin for Stroke Prevention in Atrial Fibrillation: A Patient-Level Meta-Analysis,"* J. Am. Coll. Cardiol., vol. 65, no. 24, pp. 2614–2623, Jun. 2015, doi: 10.1016/j.jacc.2015.04.025.

[59] Masci Alessandro, Barone Lorenzo, Dedè Luca, Fedele Marco, Tomasi Corrado, Quarteroni Alfio, Corsi Cristiana, "The Impact of Left Atrium Appendage Morphology on Stroke Risk Assessment in Atrial Fibrillation: A Computational Fluid Dynamics Study," Frontiers in Physiology, 2019, 10.3389/fphys.2018.01938

[60] Bosi Giorgia Maria, Cook Andrew, Rai Rajan, Menezes Leon J., Schievano Silvia, Torii Ryo, Burriesci Gaetano, *"Computational Fluid Dynamic Analysis of the Left Atrial Appendage to Predict Thrombosis Risk,"* Frontiers in Cardiovascular Medicine, 2018 10.3389/fcvm.2018.00034

[61] D. Tanne,, E. Bertrand, P. Pibarot & R. Rieu (2008) *"Asymmetric flows in an anatomical-shaped left atrium by 2C-3D+T PIV measurements,"* Computer Methods in Biomechanics and Biomedical Engineering, 11:sup001, 209-211, DOI: 10.1080/10255840802298943

[62] Huang, X.; Chrisman, J. D.; Zacharia, N. S. *Omniphobic Slippery Coatings Based on Lubricant-Infused Porous Polyelectrolyte Multilayers*. *ACS Macro Lett.* 2013, *2*, 826– 829, DOI: 10.1021/mz400387w

[63] Wong T.S *"Bioinspired self-repairing slippery surfaces with pressure-stable omniphobicity".* Nature (September 2011) 477: 443-447

[64] Sunny, S.; Vogel, N.; Howell, C.; Vu, T. L.; Aizenberg, J. *Lubricant-Infused Nanoparticulate Coatings Assembled by Layer-by-Layer Deposition*. *Adv. Funct. Mater.* 2014, *24*, 6658– 6667, DOI: 10.1002/adfm.201401289

[65] Geraldi, N.R., Guan, J.H., Dodd, L.E. *et al. Double-sided slippery liquid-infused porous materials using conformable mesh*. *Sci Rep* 9, 13280 (2019). https://doi.org/10.1038/s41598-019-49887-3

[66] R. Zhang and Y. Zhang, *"An Experimental Study of Pulsatile Flow in a Compliant Aortic Root Model under Varied Cardiac Outputs,"* Fluids, vol. 3, no. 4, p. 71, Dec. 2018, doi: 10.3390/fluids3040071.

[67] H. Ujiie et al., *"Effects of size and shape (aspect ratio) on the hemodynamics of saccular aneurysms: a possible index for surgical treatment of intracranial aneurysms,"* 8 © 2020 by ASME Neurosurgery, vol. 45, no. 1, pp. 119–129; discussion 129-130, Jul. 1999.

[68] H. Ujiie, Y. Tamano, K. Sasaki, and T. Hori, *"Is the Aspect Ratio a Reliable Index for Predicting the Rupture of a Saccular Aneurysm?,"* Neurosurgery, vol. 48, no. 3, pp. 495–503, Mar. 2001, doi: 10.1097/00006123- 200103000-00007.

[69] O. Bazan and J. P. Ortiz, *"Duration of Systole and Diastole for Hydrodynamic Testing of Prosthetic Heart Valves: Comparison Between ISO 5840 Standards and in vivo Studies,"* Braz. J. Cardiovasc. Surg., vol. 31, no. 2, pp. 171–173, 2016, doi: http://dx.doi.org/10.5935/1678-9741.20160036.

[70] Y. C. Fung, *Biomechanics: Circulation*. Springer Science & Business Media, 2013.

[71] Kompenhans, Juergen & Raffel, M., et al,. "*Particle Image Velocimetry in Aerodynamics: Technology and Applications in Wind Tunnels."* International Conference on Optical Technology and Image Processing in Fluid, Thermal and Combustion Flow, December 1999

[72] Gerber B., Singh J., Zhang Y., Liou, W. *"A computer simulation of short-term adaptations of cardiovascular hemodynamics in microgravity".* Computers in Biology and Medicine, (2018), 102, 86-94 .

[73] Zhang, Y., Liou, W. W., & Gupta, V., *"Modeling of high sodium intake effects on left ventricular hypertrophy".* Computers in Biology and Medicine, 2015, 58, (1 March 2015), 31–39

[74] Oh J.K. *"Established and Novel Clinical Applications of Diastolic Function Assessment by Echocardiography".* Circulation American Heart Association (July 2011) 4(4): 444-455

[75] De A. *"Echocardiographic assessment of diastolic function"* Journal of the Indian Academy of Echocardiography & Cardiovascular Imaging (December 2017) 1(3): 214-221

[76] Gutierrez C. *"Diastolic Heart Failure: Challenges of Diagnosis and Treatment"*. American Family Physician, (June 2004) 1:69(11): 2609-2617

[77] Kim T.S. "*Role of Echocardiography in Atrial Fibrillation*" Journal of Cardiovascular Ultrasound (June 2011) 19(2): 51-61

[78] Alberts B, Johnson A, Lewis J, et al. *Molecular Biology of the Cell. 4th edition*. New York: Garland Science; 2002. Blood Vessels and Endothelial Cells.